MODELING, SIMULATION, AND ESTIMATION OF OPTICAL TURBULENCE

DISSERTATION

Byron Paul Formwalt, Major, USAF

AFIT/GE/ENG/DSG-06S

DEPARTMENT OF THE AIR FORCE
AIR UNIVERSITY

AIR FORCE INSTITUTE OF TECHNOLOGY

Wright-Patterson Air Force Base, Ohio

Modeling, Simulation, and Estimation of Optical Turbulence

DISSERTATION

Presented to the Faculty

Department of Electrical and Computer Engineering

Graduate School of Engineering and Management

Air Force Institute of Technology

Air University

Air Education and Training Command

In Partial Fulfillment of the Requirements for the

Degree of Doctor of Philosophy in Electrical Engineering

Byron Paul Formwalt, B.S.E.E., M.S.E.E.

Major, USAF

December 2006

Modeling, Simulation, and Estimation of Optical Turbulence

Byron Paul Formwalt, B.S.E.E., M.S.E.E.

Major, USAF

Approved:

_____   24 Jan 07

Dr. Stephen C. Cain   date

Dissertation Advisor
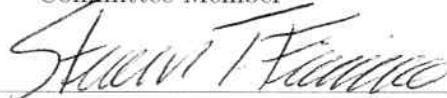
_____   31 JAN 07

Lt Col Matthew E. Goda, Ph.D.   date

Committee Member
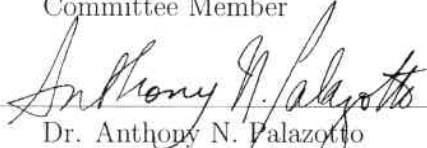
_____   7 FEB 07

Lt Col Steven T. Fiorino, Ph.D.   date

Committee Member
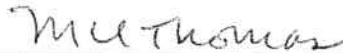
_____   8 feb 07

Dr. Anthony N. Palazotto   date

Dean-Appointed Representative

Accepted:

_____   26 Feb 07

Marlin U. Thomas   Date

Dean, Graduate School of Engineering and Management

Abstract

This dissertation documents three new contributions to simulation and modeling of optical turbulence. The first contribution is the formalization, optimization, and validation of a modeling technique called successively conditioned rendering (SCR). The SCR technique is empirically validated by comparing the statistical error of random phase screens generated with the technique. The second contribution is the derivation of the covariance delineation theorem, which provides theoretical bounds on the error associated with SCR. It is shown empirically that the theoretical bound may be used to predict relative algorithm performance. Therefore, the covariance delineation theorem is a powerful tool for optimizing SCR algorithms. For the third contribution, we introduce a new method for passively estimating optical turbulence parameters, and demonstrate the method using experimental data. The technique was demonstrated experimentally, using a 100 m horizontal path at 1.25 m above sun-heated tarmac on a clear afternoon. For this experiment, we estimated $C_n^2 \approx 6.01 \cdot 10^{-9}\, \mathrm{m}^{-\frac{2}{3}}$, $l_0 \approx 17.9\, \mathrm{mm}$, and $L_0 \approx 15.5\, \mathrm{m}$.

Acknowledgements

Table of Contents

List of Figures

List of Tables

List of Symbols

List of Abbreviations

MODELING, SIMULATION, AND ESTIMATION OF OPTICAL
TURBULENCE

1. Introduction

Applications dealing with optical turbulence are numerous in industry and the Department of Defense. This research introduces three new contributions to help advance the state of the art. The following sections provide a roadmap for this document, as well as justification for research it represents in context of Air Force needs.

1.1 Organization

The following is a list of chapter descriptions:

- Chapter 1: Serves as a roadmap for the document, and provides justification for this research.

- Chapter 2: Presents a modeling technique called SCR and derives a theorem to support the technique. Empirical data are used to validate the findings. The contents of this chapter have been published in a peer-reviewed journal. [9]

- Chapter 3: Presents a method for estimating optical turbulence parameters from imaging data. The method is demonstrated using physical data from field experiments. The contents of this chapter have been submitted to the journal, *Applied Optics*, and are currently undergoing peer review.

- Chapter 4: Provides a final overview of this research by reviewing results and conclusions from Chapters 2 and 3. Outlines the direction of future work by this author.

- Appendix A: Justifies use of rectlinear phase integration through turbulent media for geometries where scintillation (receiver irradiance fluctuation) effects are negligible.

1.2 Contributions

There are three contributions presented in Chapters 2 and 3:

- Contribution 1: Formalization, optimization, and validation of SCR as a technique for modeling spatially homogenous and isotropic random fields in n-dimensions. SCR is shown to be a statistical filter process with $\mathcal{O}(n)$ computational complexity, where n represents the number of spatial points at which the field is to be simulated. (Found in Chapter 2).

- Contribution 2: Proof of the covariance delineation theorem, which makes provisions for computing a least upper bound on the error incurred from the first level of SCR. Its use precludes any need for costly empirical evaluation while optimizing a particular SCR algorithm. (Found in Chapter 2).

- Contribution 3: Derivation and implementation of an estimation technique for obtaining optical turbulence model parameters. Finite outer scale and non-zero inner scale are estimated simultaneous to the refractive index structure constant. The estimation technique is demonstrated using physical data collected from a field experiment. (Found in Chapter 3).

1.3 Value to the Air Force

Contributions 1 and 2 are good for rapidly simulating extensible phase screens to an arbitrary level of detail. Immediate Air Force applications include characterizing performance of optical sensors and algorithms. Contribution 3 is an economical solution for characterizing optical turbulence in support of field tests of Air Force optical systems. Key advantages are support of a wider range of propagation path lengths at a fraction of the cost for scintillometer-based alternatives. Because the sensing technique is passive, it is inherently eye-safe.

1.4 Summary of Prior Contributions and Theory

Before delving into the details for the new contributions presented in this work, the reader may wish to skim this section as a primer on theory related to previous works published. Each subsection discusses material as it relating to a single contribution. Use of SI units is implied everywhere in this document, unless specified otherwise.

1.4.1 Contribution 1.

This contribution consists of a technique for simulating phase screens by successively conditioned rendering. Some early works published on phase screen simulation relied upon Cholesky decomposition. The recipe for this technique, based on is available in References [24] and [25]. While the results are statistically error free, the Cholesky-based approach becomes computationally intractable for applications requiring phase screens with a large number of samples.

In 1992, Lane, *et al*, used a midpoint displacement algorithm from the computer graphics community and applied it to Kolmogorov phase screen generation [16]. Lane showed that the algorithm was significantly faster than Fourier-based techniques, but less accurate. The midpoint displacement algorithm is a form of statistical interpolation, whereby each new interpolate is obtained by adding a zero-mean random variable to the corresponding interpolate obtained using linear interpolation. In this paper, Lane also introduced a more efficient Fourier technique that uses a non-uniform sampling grid to incorporate subharmonic frequencies. Fewer samples are used overall, resulting in a faster simulation than the one presented in [25], [24], yet similar accuracy is obtained by adding more samples at lower spatial frequencies. The downside is that the fast Fourier transform (FFT) algorithm cannot be used with nonuniform sampling grids–a fact which cuts down on the overall computational efficiency of the method. As a followup study, in 1999, Harding, *et al* [13] provided a more in-depth theoretical explanation of the midpoint displacement algorithm as it was applied to the problem of phase screen generation. Harding also examined slight variations of the original algorithm, and characterized the computational efficiency of the algorithm. In 2003,

Peterson and Mozurkewich [23] introduced an algorithm that applied Lane's midpoint displacement technique to selectively interpolate a large-scale phase screen for multiple regions of interest. They also added the concept of extending the phase screen arbitrarily in any direction. By contrast to prior contributions, the work presented in this document offers a purely covariance-based Bayesian probability approach to statistical interpolation. Furthermore, a variant of Lane's algorithm is introduced, which improves both the efficiency and accuracy for this class of algorithm.

1.4.2 Contribution 2.   The covariance delineation theorem is a completely original contribution unrelated to prior works. Prior to introducing the theorem, we provide as reference a few definitions specific to this text. These definitions are formally introduced in Section 2.4:

- Correlated Random Set: *A countable set of correlated random variables.*

- Conditional Independence: *Statistical independence of two or more random variables under a specific set of conditions.*

- Random Estimate: *A random variable whose statistics approximate the statistics of another random variable.*

Readers without a strong background in linear algebra or probability and statistics may find it helpful to obtain copies of References [22] and [27] to facilitate understanding of the proof for this theorem. Both texts are excellent pedagogical references and use similar notation as this document.

1.4.3 Contribution 3.   This contribution is a new approach to estimating optical turbulence parameters. We begin by defining what these parameters are and discuss their historical importance in optical turbulence modeling. After that, we provide a synopsis of other practical methods for estimating optical turbulence parameters found in the literature.

4

1.4.3.1 Optical Turbulence Parameters. The material for this section comes directly from Chapter 3 of *Laser Beam Propagation Through Random Media* by Andrews and Phillips [2]. Optical turbulence refers to spatial fluctuations in the refractive index throughout a volume of atmosphere. These fluctuations are thought to be caused primarily by temperature fluctuations, but are also dependent on optical wavelength, atmospheric pressure, and relative humidity [4]. Such fluctuations occur at random and with some amount of spatial correlation. We refer to the random spatial variations in the refractive index collectively as a correlated random field. A common practice in modeling optical turbulence is to assume local homogeneity and isotropy in two or more spatial dimensions. The resultant field is called a spatially correlated homogenous and isotropic random field. The statistics relating points within such a field are functions only of the distance between points, and implicitly do not depend on relative orientation or absolute position of points within the field.

In 1941, Kolmogorov developed a statistical model for turbulence, in which he related the statistical structure in wind velocity measured at two points to the distance between them. The turbulence parameter, L_0, was used to denote the largest sized eddy with homogenous and isotropic statistical structure. L_0 is known as the outer scale of turbulence. Another parameter, l_0, was defined as the scale for which turbulent eddies lose all their energy to viscous forces. l_0 is called the inner scale of turbulence. Kolmogorov defined the following 2/3 power law valid for distances of separation less than L_0 and greater than l_0:

$$\begin{aligned} D_V(R) &\triangleq E\left[\left((V(\boldsymbol{P_2}) - E\left[V(\boldsymbol{P_2})\right]) - (V(\boldsymbol{P_1}) - E\left[V(\boldsymbol{P_1})\right])\right)^2\right] \\ &= E\left[(V(\boldsymbol{P_2}) - V(\boldsymbol{P_1}))^2\right] \\ &= C_V^2 R^{\frac{2}{3}}, \end{aligned}$$

(1.1)

where

$$R \triangleq |\boldsymbol{P_2} - \boldsymbol{P_1}|,$$

(1.2)

5

for two points, $\boldsymbol{P}_1$ and $\boldsymbol{P}_2$, in Euclidean three-space. $D_V(R)$ is the structure function for a statistically homogenous and isotropic random velocity field, $E[\cdot]$ denotes the ensemble average of a random quantity, V represents velocity, and C_V^2 is the velocity structure constant.

The inertial range is defined as a subinterval of the range of distances between the inner and outer scales of turbulence:

$$l_0 \ll R \ll L_0. \tag{1.3}$$

Since this relationship is rather ambiguous, in practice, we use an alternate definition for the inertial range based on a comparison of the Kolmogorov model to more recent theory:

$$R : \left\{ \log_{10} \left\{ \frac{l_0}{R} \right\} < -1 \right\} \bigcap \left\{ \log_{10} \left\{ \frac{L_0}{R} \right\} > 1.5 \right\}. \tag{1.4}$$

The Kolmogorov model for turbulence is only considered valid for the inertial range. In 1962, Obukhov applied Kolmogorov's model to describe the statistical structure of temperature fluctuations. He hypothesized that velocity and thermal structure would have proportionate statistical structures, because the energy represented by the turbulent flow of air results almost entirely from fluctuations in temperature. External fluctuations in pressure can also induce turbulent air flow. For purposes of this research, we assume an environment that supplies nearly constant atmospheric pressure and relative humidity, such that the corresponding effects on refractive index fluctuations are negligible. Obukhov published the following statistical model for temperature fluctuations on the inertial subrange:

$$D_T(R) = C_T^2 R^{\frac{2}{3}}, \tag{1.5}$$

where $D_T(R)$ is the structure function for temperature (T) and C_T^2 is the thermal structure constant. Andrews and Phillips use the following simplified model to relate

6

temperature fluctuations to refractive index fluctuations:

$$n(\boldsymbol{P}) = 1 + 79 \times 10^{-6} \frac{P(\boldsymbol{P})}{T(\boldsymbol{P})}, \tag{1.6}$$

where $P(\boldsymbol{P})$ and $T(\boldsymbol{P})$ represent pressure and temperature, respectively, at some point, $\boldsymbol{P}$ in Euclidean three-space. A wavelength of $\lambda = 500\,\text{nm}$ is assumed. Relative humidity is not specified by the text cited. Units of pressure for this expression are millibars. To extend Kolmogorov's 2/3 power law to refractive index fluctuations, one has to make additional assumptions and approximations. First, we express the structure function for the refractive index:

$$
\begin{aligned}
D_n(R) &\triangleq E[(n(\boldsymbol{P_2}) - n(\boldsymbol{P_1}))^2] \\
&\approx C_n^2 R^{\frac{2}{3}},
\end{aligned}
\tag{1.7}
$$

where C_n^2 is the refractive index structure constant. Next, we apply (1.7) to (1.6). Setting $K = 79 \times 10^{-6} P$, we have

$$
\begin{aligned}
D_n(R) &= E\left[\left(\left(1 + \frac{K}{T(\boldsymbol{P_2})}\right) - \left(1 + \frac{K}{T(\boldsymbol{P_1})}\right)\right)^2\right] \\
&= K^2 E\left[\left(\frac{1}{T(\boldsymbol{P_2})} - \frac{1}{T(\boldsymbol{P_1})}\right)^2\right] \\
&= K^2 E\left[\frac{(T(\boldsymbol{P_1}) - T(\boldsymbol{P_2}))^2}{(T(\boldsymbol{P_1})T(\boldsymbol{P_2}))^2}\right].
\end{aligned}
\tag{1.8}
$$

Define

$$T(\boldsymbol{P}) = T_0 + T_1(\boldsymbol{P}), \tag{1.9}$$

where $T_0 = E[T]$ is the mean spatial temperature for the turbulent volume of interest. Next, we assume that T obeys a normal distribution with $E^2[T] \gg \text{var}[T]$, and express

7

approximate

$$
\begin{aligned}
D_n(R) &\approx K^2 \frac{E\left[(T(\boldsymbol{P_1}) - T(\boldsymbol{P_2}))^2\right]}{E\left[(T(\boldsymbol{P_1})T(\boldsymbol{P_2}))^2\right]} \\
&= K^2 \frac{D_T(R)}{E\left[(T(\boldsymbol{P_1})T(\boldsymbol{P_2}))^2\right]} \\
&= K^2 \frac{D_T(R)}{E\left[((T_0 + T_1(\boldsymbol{P_1}))(T_0 + T_1(\boldsymbol{P_2})))^2\right]} \\
&= K^2 \frac{D_T(R)}{E\left[T_0^4 + T_0^2(T_1(\boldsymbol{P_1}) + T_1(\boldsymbol{P_2}))^2 + (T_1(\boldsymbol{P_1})T_1(\boldsymbol{P_2}))^2\right]}.
\end{aligned}
\tag{1.10}
$$

Since the thermal fluctuations are expected to be small compared to the mean environmental temperature given in units of Kelvin, we can write $|T_0| \gg |T_1(\boldsymbol{P_1})|$, and then further approximate

$$
\begin{aligned}
D_n(R) &\approx K^2 \frac{D_T(R)}{E\left[T_0^4\right]} \\
&= K^2 \frac{D_T(R)}{T_0^4} \\
&= K^2 \frac{C_T^2 R^{\frac{2}{3}}}{T_0^4}.
\end{aligned}
\tag{1.11}
$$

Therefore, it is implied that

$$
\begin{aligned}
C_n^2 &= K^2 \frac{C_T^2}{T_0^4} \\
&= \left(\frac{79 \times 10^{-6} P}{T_0^2}\right)^2 C_T^2.
\end{aligned}
\tag{1.12}
$$

The covariance spectrum, $\Phi_n(\kappa)$, for the refractive index in a statistically homogenous and isotropic random field is related to the statistical field structure, $D_n(R)$, by

$$
D_n(R) = 8\pi \int_0^\infty \kappa^2 \Phi_n(\kappa) \left(1 - \frac{\sin(\kappa R)}{\kappa R}\right),
\tag{1.13}
$$

8

where κ denotes scalar spatial frequency. The associated spectrum for the Kolmogorov model within the inertial range is given by

$$\Phi_n(\kappa) = 0.033 C_n^2 \kappa^{-\frac{11}{3}}.$$ (1.14)

Several years later, a more accurate model for the spectrum of refractive index fluctuations emerged, called the von Kármán spectrum:

$$\Phi_n(\kappa) = 0.033 C_n^2 \exp\left\{-\frac{\kappa^2 l_0^2}{5.92}\right\} \left(\kappa^2 + (2\pi)^2 L_0^{-2}\right)^{-\frac{11}{6}},$$ (1.15)

which is valid for $0 \leq R, \kappa < \infty$ and incorporates parameters l_0 and L_0 in addition to C_n^2. In this contribution, we use derive an covariance-based optical technique to estimate all three parameters of this model simultaneously.

1.4.3.2 Alternative Estimation Methods. The majority of pre-existing turbulence parameter estimation techniques rely on measurements of scintillation. Scintillation is often defined as the fluctuation in received irradiance due to atmospheric turbulence. Scintillation is affected by all three parameters (l_0, L_0, and C_n^2) [30]. The scintillation index is defined as [1]

$$\sigma_I^2 \triangleq \frac{E[I^2]}{E^2[I]} - 1,$$ (1.16)

where I represents irradiance. For an unbounded plane wave propagating through weak turbulence conditions ($\sigma_I^2 < 1$), we have [1]

$$\sigma_{I_{weak}}^2 \approx 1.23 C_n^2 k^{\frac{7}{6}} \Delta z^{\frac{11}{6}},$$ (1.17)

which is also known as the Rytov variance. In this expression, Δz is the propagation distance, and $k = \frac{2\pi}{\lambda}$. For Rytov variances much greater than unity, $\sigma_{I_{weak}}^2$ overestimates σ_I^2, and turbulence fluctuations are said to be saturated [1]. Typical methods

9

for determining C_n^2 and L_0 use this $\sigma_{I_{weak}}^2$ to describe irradiance fluctuations received from a collimated laser propagating through weak turbulence.

As turbulence conditions become stronger $(\sigma_{I_{weak}}^2 > 3)$, the inner scale has an increasing effect on the scintillation index. The most recent contribution published uses a model for the scintillation index that is valid for all turbulence conditions for large-aperture receivers. The model takes the form [30]

$$\sigma_I^2(l_0, L_0, C_n^2, D) = \exp\left\{\sigma_{\ln\{I_{large}\}}^2(l_0, L_0, C_n^2, D) + \sigma_{\ln\{I_{small}\}}^2(l_0, C_n^2, D)\right\} - 1, \quad (1.18)$$

where $\sigma_{\ln\{I_{large}\}}^2$ is the variance in the log of the irradiance due to large-scale fluctuations, and $\sigma_{\ln\{I_{small}\}}^2$ describes the same quantity, except for small-scale irradiance fluctuations. D is the diameter of the aperture. By using three different sized apertures, Vetelino, *et al*, were able to conduct an experiment, in which they obtained the first simultaneous measurements of l_0, L_0, and C_n^2 [30]. In order to obtain enough optical scintillation to measure all three parameters, a 1.5 km path was used. Three separate receiving apertures, and 150 mw of 1.55 μm collimated laser radiation were required for this active experiment. Until now, there has been no other attempt to estimate all three parameters simultaneously.

By contrast, this document introduces a method of simultaneously estimating the same parameters passively, using a single receiving aperture, requiring an optical path length of only 100 m through turbulence. Instead of using scintillation phenomenology, as does the majority of prior literature, this technique relies on theory derived from the tilt covariance expressions relating a one-dimensional nonlinearly-distributed array of point sources.

2. Optimized Phase Screen Modeling for Optical Turbulence

Atmospheric turbulence is a fundamental factor contributing to the imaging quality obtainable by ground-based astronomy. Imaging through atmospheric turbulence is a process commonly modeled by inserting a random phase screen directly over the aperture of the imaging system, with zero or more additional phase screens distributed along the optical path. Therefore, a key component to modeling astronomical observations is the means to quickly and accurately simulate random phase screens. In their recent text, Roggemann and Welsh outline a method for simulating random phase screens directly by using a phase covariance function [24]. This direct covariance method suffers practical memory limitations scaling with $\mathcal{O}(n^4)$, where n refers to the number of samples per axis. In 1992, Lane et al introduced a fast and practical method for statistically interpolating existing phase screens to a finer resolution [16]. His algorithm is based on the midpoint displacement technique which is borrowed from the computer graphics community. Six years later, in collaboration with Lane and in association with the University of Canterbury in New Zealand, Harding et al optimized the algorithm for speed and accuracy with respect to the size of the interpolator [13]. Harding et al also presented a more detailed derivation of the algorithm. Both efforts focused on applying the midpoint displacement algorithm to Kolmogorov phase screens.

2.1 Roadmap

This chapter builds on prior works by presenting an alternative statistical interpolation algorithm which is useful for modeling phase with a finite outer scale. More importantly, this chapter introduces a theorem which gives a theoretical basis for the statistical interpolator, and simultaneously generates a criterion for optimizing interpolators by non-empirical means. While this chapter applies the theorem only to random phase screens, the theorem is also valid for any other simulation that implements SCR. First, we provide a mathematical introduction to SCR. After the theorem

11

is stated, it is proven, and later empirically validated by comparing two alternative statistical interpolators.

2.2 Successively Conditioned Rendering

Let $\mathbb{W}$ be an ordered set of correlated scalar random variables, and let $\mathbb{V}$ be a corresponding ordered set of scalar realizations. In particular, if we are given a set of realizations, $\mathbb{V} \triangleq \{v_1, v_2, v_3, \ldots, v_M\}$, for M corresponding correlated random variables, $\mathbb{W} \triangleq \{w_1, w_2, w_3, \ldots, w_M\}$, we wish to simulate one realization of the random variable, $w_0 \notin \mathbb{W}$, by rendering a corresponding value $v_0 \notin \mathbb{V}$. After v_0 has been assigned, we would set $w_{M+1} \leftarrow w_0$, $v_{M+1} \leftarrow v_0$, and $M \leftarrow M + 1$. That is to say, we would union $\{w_0\}$ with $\mathbb{W}$, before considering a new random variable w_0. This process is referred to as successively conditioned rendering (SCR). In this chapter we are concerned with random phase as it relates to imaging applications. Imaging processes are inherently insensitive to piston and residual spatial phase is predominately modeled by the multivariate normal distribution [24]. Therefore, we will restrict our SCR analysis to the zero-mean multivariate normal distribution. Let $\boldsymbol{v}$ be a column vector containing all of the elements of the set $\mathbb{V}$ and let $\boldsymbol{w}$ be a corresponding vector containing all the elements of $\mathbb{W}$. The joint probability density for the set of random variables, $\mathbb{W}$, defined for a particular set of realizations, $\mathbb{V}$, is given by

$$p_{\boldsymbol{w}}(\boldsymbol{v}) \triangleq \left[(2\pi)^M |\boldsymbol{C}|\right]^{-\frac{1}{2}} \exp\left\{-\tfrac{1}{2}\boldsymbol{v}^T \boldsymbol{C}^{-1} \boldsymbol{v}\right\}, \tag{2.1}$$

where $\boldsymbol{C}$ represents the covariance matrix describing $\mathbb{W}$, and is defined by $\boldsymbol{C} \triangleq E[(\boldsymbol{w} - E[\boldsymbol{w}])(\boldsymbol{w} - E[\boldsymbol{w}])^T] = E[\boldsymbol{w}\boldsymbol{w}^T]$. We define $\boldsymbol{w}_0$ and $\boldsymbol{v}_0$ to be the column vectors $\boldsymbol{w}_0 \triangleq [w_0, \boldsymbol{w}^T]^T$ and $\boldsymbol{v}_0 \triangleq [v_0, \boldsymbol{v}^T]^T$. Similarly, we define the joint pdf describing $w_0 \bigcup \mathbb{W}$ as

$$p_{\boldsymbol{w}_0}(\boldsymbol{v}_0) \triangleq \left[(2\pi)^{M+1} |\boldsymbol{C}_0|\right]^{-\frac{1}{2}} \exp\left\{-\tfrac{1}{2}\boldsymbol{v}_0^T \boldsymbol{C}_0^{-1} \boldsymbol{v}_0\right\}, \tag{2.2}$$

where $C_0 \equiv E[w_0 w_0^T]$. Through Bayes' rule, the conditional pdf of w_0, given w is defined as

$$
\begin{aligned}
p_{w_0|w}(v_0) &= \frac{p_{w_0}(v_0)}{p_w(v)} \\
&= \frac{\left[(2\pi)^{M+1}|C_0|\right]^{-\frac{1}{2}} \exp\left\{-\frac{1}{2}v_0^T C_0^{-1} v_0\right\}}{\left[(2\pi)^M |C|\right]^{-\frac{1}{2}} \exp\left\{-\frac{1}{2}v^T C^{-1} v\right\}} \\
&= K_1(v) \exp\left\{-\frac{1}{2}v_0^T C_0^{-1} v_0\right\},
\end{aligned}
\tag{2.3}
$$

where we have conveniently defined

$$
K_1(v) \triangleq \left[\frac{|C|}{2\pi|C_0|}\right]^{\frac{1}{2}} \exp\left\{\frac{1}{2}v^T C^{-1} v\right\}
\tag{2.4}
$$

to encapsulate all the coefficients that do not depend on w_0. Next, we define $S_0 \triangleq C_0^{-1} = \{s_{i,j}\}$, where $i, j \in \{0, 1, 2, \ldots, M\}$. Then, the quantity $v_0^T C_0^{-1} v_0$, taken from the argument of the exponential from (2.3) expands to

$$
\begin{aligned}
v_0^T C_0^{-1} v_0 &= \sum_{i=0}^{M} v_i \sum_{j=0}^{M} v_j s_{i,j} \\
&= \sum_{i=0}^{M} \sum_{j=0}^{M} v_i v_j s_{i,j} \\
&= v_0^2 s_{0,0} + \sum_{i=1}^{M} v_i v_0 s_{i,0} + \sum_{j=1}^{M} v_0 v_j s_{0,j} + K_2(v),
\end{aligned}
\tag{2.5}
$$

where we have isolated the terms containing v_0 and relegated the remaining terms into $K_2(v)$. By definition, C_0 is symmetric [27]. Therefore, its inverse, S_0, is also symmetric. This property allows us to combine cross terms, resulting in the expression

$$
v_0^T C_0^{-1} v_0 = v_0^2 s_{0,0} + 2\sum_{i=1}^{M} v_i v_0 s_{i,0} + K_2(v).
\tag{2.6}
$$

13

Completing the square would require a conversion of the form

$$ax^2 + bx + c = \left(a^{\frac{1}{2}}x + \frac{b}{2a^{\frac{1}{2}}} \right)^2 + c - \frac{b^2}{4a}, \tag{2.7}$$

substituting $x \leftarrow v_0$. Consolidating the remaining terms into a new function, $K_3(v)$, *which does not depend on v_0*, enables us to compactly express the completed square as

$$
\begin{aligned}
v_0^T C_0^{-1} v_0 &= \left(s_{0,0}^{\frac{1}{2}} v_0 + s_{0,0}^{-\frac{1}{2}} \sum_{i=1}^{M} v_i s_{i,0} \right)^2 + K_3(v) \\
&= s_{0,0}^2 \left(v_0 + s_{0,0}^{-1} \sum_{i=1}^{M} v_i s_{i,0} \right)^2 + K_3(v).
\end{aligned}
\tag{2.8}
$$

The resulting form for the conditional pdf from (2.3) is

$$p_{w_0|w}(v_0) = K_4(v) \exp \left\{ -\frac{1}{2} s_{0,0} \left(v_0 + s_{0,0}^{-1} \sum_{i=1}^{M} v_i s_{i,0} \right)^2 \right\}, \tag{2.9}$$

which we immediately recognize as a univariate normal density with the following parameters for the mean and standard deviation:

$$
\begin{aligned}
\mu_0 &= - s_{0,0}^{-1} \sum_{i=1}^{M} v_i s_{i,0} \\
\sigma &= s_{0,0}^{-\frac{1}{2}}.
\end{aligned}
\tag{2.10}
$$

From this form, it is apparent that the conditional mean is simply a weighted sum of the conditional data, and that the conditional standard deviation is related to the first diagonal element of the inverse of the covariance matrix. For applications where C is reused many times, it will suffice to pretabulate the first row of C^{-1}, allowing these cached values to be reused as linear filter taps for obtaining the parameters defined in (2.10). Under such conditions, this problem reduces to complexity $\mathcal{O}(M)$.

14

2.3 *Statistical Interpolation*

References [13,16] both describe the resolution enhancement as a two-step recursive process, where the first step is linear interpolation, and the second step is random midpoint displacement. This chapter introduces a new perspective on achieving the same result. The two steps are combined into a single step, called statistical interpolation, and is based on SCR. We begin with a set of M phase samples uniformly distributed over a coarse-resolution 2-D rectangular grid. It is presumed that phase is statistically homogenous and isotropic over the local area defined by the phase screen. This assumption allows us to express phase covariance as a function of separation between two points in the aperture without regard to absolute position or relative orientation. We define $B_\psi(R_\perp)$ to be the phase covariance between two points in the aperture separated by the distance, $R_\perp$. The task of statistical interpolation is to use our knowledge of existing phase samples to simulate additional phase values at locations between the coarse-resolution grid points. A mathematically pure solution is to apply SCR to render each additional point in succession, with an increasingly large set of prior data. Unfortunately, this is as computationally complex as applying the direct method to generate a fine-resolution phase screen.

The mathematically tractable approximation originally proposed by Lane is to limit the pool of prior data to a subset of $\mathbb{V}$, based on our knowledge of the covariance function. The phase covariance functions for all published turbulence spectra are positive and monotonically decreasing with respect to $R_\perp$. This property implies that the nearest neighbors of a point are most highly correlated in phase. This is why Lane's method relies on the subset of prior data represented by the m nearest neighbors when rendering a new point on a finer resolution grid. Whereas Lane and Harding, *et al*, pursued this idea with midpoint displacement, in this chapter, information limited SCR is applied instead. Otherwise, the algorithms are similar.

What has been lacking up until now is theoretical proof of why these algorithms produce such accurate phase simulations using incomplete information. Furthermore, it is desirable to quantify how well one interpolation scheme is expected to perform as compared to another. If such quantification can be achieved by a simple formulation, rather than by mass simulation, one would be able to quickly optimize such an interpolator. The following theorem embodies the vital link between theory and practice.

Definition 2.1 (Correlated Random Set). *A countable set of correlated random variables.*

Definition 2.2 (Conditional Independence). *Statistical independence of two or more random variables under a specific set of conditions.*

Definition 2.3 (Random Estimate). *A random variable whose statistics approximate the statistics of another random variable.*

Theorem 2.1 (Covariance Delineation Theorem). *Consider a real-valued correlated random set, $\mathbb{W} \triangleq \{w_1, w_2, w_3, ...w_M\}$, for which all statistical moments are known. Consider also, a particular corresponding realization, $\mathbb{V} \triangleq \{v_1, v_2, v_3, ...v_M\}$, of the correlated random set, $\mathbb{W}$. Then, consider a particular correlated random subset, $\mathbb{W}^\iota \triangleq \{w_1^\iota, w_2^\iota, w_3^\iota, \ldots, w_{m-1}^\iota\} \subset \mathbb{W}$, with corresponding realization, $\mathbb{V}^\iota \triangleq \{v_1^\iota, v_2^\iota, v_3^\iota, \ldots, v_{m-1}^\iota\} \subset \mathbb{V}$, which is collectively referred to as information source ι. We wish to examine an additional real-valued random variable, $w_0^\iota \equiv w_0 \notin \mathbb{W}$, for which all statistical moments are known, but for which no known realization exists corresponding to the members of $\mathbb{V}$. The statistically correct way to simulate w_0 is by random selection according to the conditional probability density function (pdf), $p_{w_0|\boldsymbol{w}}(w_0|\boldsymbol{w})$, where $\boldsymbol{w}$ is a vector containing all the elements of $\mathbb{W}$. In certain applications where computational efficiency is at a premium, it may be more desirable to introduce an acceptable level of error by restricting the amount prior data used to*

condition the pdf of w_0. Consider the case where w_0 is approximately simulated according to the conditional pdf, $p_{\hat{w}_0^t|\boldsymbol{w}^t}(w_0|\boldsymbol{w}^t)$, where $\boldsymbol{w}^t$ is a vector containing all the elements of $\mathbb{W}^t$. The random variable, $\hat{w}_0$, described by this pdf is a random estimate of w_0. We define the second-order statistical error of this random estimate (SERE) as the normalized root mean squared error between the second-order statistics of w_0 and the second-order statistics of $\hat{w}_0^t$ with respect to $\mathbb{W}$:

$$
\begin{aligned}
\mathcal{E}_\iota &\triangleq \left[E[(w_0 - E[w_0])^2] \sum_{i=0}^{M} E[(w_i - E[w_i])^2] \right]^{-\frac{1}{2}} \\
&\quad \times \left[\sum_{i=0}^{M} \left| (E[w_0 w_i] - E[w_0]E[w_i]) - (E[\hat{w}_0^t w_i] - E[\hat{w}_0^t]E[w_i]) \right|^2 \right]^{\frac{1}{2}} \\
&= \left[E[(w_0 - E[w_0])^2] \sum_{i=0}^{M} E[(w_i - E[w_i])^2] \right]^{-\frac{1}{2}} \\
&\quad \times \left[\sum_{i=0}^{M} \left| E[w_0 w_i] + E[w_i](E[\hat{w}_0^t] - E[w_0]) - E[\hat{w}_0^t w_i] \right|^2 \right]^{\frac{1}{2}} .
\end{aligned}
\tag{2.11}
$$

Define the $\boldsymbol{C}$ to be the covariance matrix, $\boldsymbol{C} \triangleq \{c_{i,j}\}$, where $c_{i,j} = E[w_i^t w_j^t] - E[w_i^t]E[w_j^t]$, for all combinations of integers $\{i,j\} \in [0, m-1] \times [0, m-1]$. Then, the least upper bound on SERE that is computable only from knowledge of $\boldsymbol{C}$ is given by

$$
\mathcal{E}_\iota \leq 2[1 - \Upsilon_\iota]^{\frac{1}{2}},
\tag{2.12}
$$

where Υ_ι is the maximum value for which

$$
\Upsilon_\iota \leq \frac{\left(\sum_{j=1}^{m-1} x_j c_{0,j} \right)^2}{c_{0,0} \sum_{i=1}^{m-1} \sum_{j=1}^{m-1} x_i c_{i,j} x_j}
\tag{2.13}
$$

is true given any set of real values, $\{x_i\}$. Υ_ι is called the statistical degree of information (SDI), and is always on the range, $[0,1]$, with $\Upsilon_\iota = 1$ corresponding to the case of perfect prior information.

17

2.5 Proof of the Covariance Delineation Theorem

We shall extend $\boldsymbol{C}$ to include an mth row and column which represent the covariances between w_i and $w_0 \cup \mathbb{W}^\iota$. Let the extended covariance matrix be denoted by $\boldsymbol{C}'$. Since each w_i except w_0 was jointly simulated according to $p_{\mathbb{W}}(\mathbb{W})$, and w_0 was approximately simulated according to $p_{\hat{w}_0|\mathbb{W}^\iota}(\hat{w}_0|\mathbb{W}^\iota)$, the only undetermined elements of $\boldsymbol{C}'$ are $c'_{0,m}$ and $c'_{m,0}$. Since $\boldsymbol{C}$ is a covariance matrix, it is necessarily symmetric. Therefore, $c'_{0,m} = c'_{m,0}$. Thus, we really only have one undetermined quantity within $\boldsymbol{C}'$.

2.5.1 Positive Semi-Definiteness of All Covariance Matrices. Next, we will show that every covariance matrix is positive semi-definite. This proof comes from a simple extension of the work found in [22] and [27]. Consider the arbitrary covariance matrix $\boldsymbol{C}$, as defined above. By definition, $\boldsymbol{C}$ is positive semi-definite if and only if

$$\boldsymbol{x}^T \boldsymbol{C} \boldsymbol{x} \geq 0, \forall \boldsymbol{x}. \tag{2.14}$$

Expanding this product into a sum of scalar multiplications, we have that

$$
\begin{aligned}
\boldsymbol{x}^T \boldsymbol{C} \boldsymbol{x} &= \sum_{i=0}^{m-1} \sum_{j=0}^{m-1} x_i E[(w_i^\iota - E[w_i^\iota])(w_j^\iota - E[w_j^\iota])] x_j \\
&= E\left[\sum_{i=0}^{m-1} \sum_{j=0}^{m-1} x_i (w_i^\iota - E[w_i^\iota])(w_j^\iota - E[w_j^\iota]) x_j \right] \\
&= E\left[\sum_{i=0}^{m-1} x_i (w_i^\iota - E[w_i^\iota]) \sum_{j=0}^{m-1} x_j (w_j^\iota - E[w_j^\iota]) \right] \\
&= E\left[\left(\sum_{i=0}^{m-1} x_i (w_i^\iota - E[w_i^\iota]) \right)^2 \right] \\
&\geq 0.
\end{aligned}
\tag{2.15}
$$

Therefore, every covariance matrix is positive semi-definite.

2.5.2 Continuity of Eigenvalues in Perturbations of a Real Symmetric Matrix.

It is necessary to establish the property of continuity of the eigenvalues from C' with respect to symmetric perturbations in elements $c'_{0,m}$ and $c'_{m,0}$. Define the perturbed covariance matrix, $Q \triangleq C' + \Delta$, where $\Delta_{0,m} = \Delta_{m,0}$ are the only non-zero elements of Δ. We wish to show that the eigenvalues of Q are continuous in $\Delta_{0,m}$. Since C' and Δ are symmetric and real, then Q is also symmetric and real. Therefore, the eigenvalues of Q are all real. The eigenvalues are defined as the roots of the polynomial $|Q - \lambda I|$. This polynomial expands to the form $|Q - \lambda I| = a_0 + a_1 \lambda + a_2 \lambda^2 + \cdots + a_{m+1} \lambda^{m+1}$. Expanding the explicit formula for the determinant found in [27], will reveal that each of the polynomial coefficients can each be expressed as a quadratic polynomial of the variable $\Delta_{0,m}$. Therefore, the coefficients $\{a_i\}$ are continuous in $\Delta_{0,m}$. The roots of a polynomial are continuous in the coefficients of that polynomial [5]. Therefore, the eigenvalues, $\{\lambda_i\}$, are necessarily continuous in the coefficients, $\{a_i\}$. Since each a_i is continuous in $\Delta_{0,m}$ and each λ_i is continuous in every a_i, then by the transitive property of continuity, each λ_i is also continuous in $\Delta_{0,m}$.

2.5.3 Existence of an Upper Bound on the Range of Positive Semi-Definiteness.

There are two cases to consider when determining the allowable range on $\Delta_{0,m}$ for which Q will be positive semi-definite. In the first case, we restrict C to be positive definite. For this case we wish to prove that there exists some interval, $[\Delta_{0,m}^L, \Delta_{0,m}^U]$, containing zero for which $\Delta_{0,m}$ results in Q being positive semi-definite. In the second case, we restrict C so that it is positive semi-definite, but not positive definite. For this case we wish to prove that $\Delta_{0,m} = 0$ is a necessary condition for Q to be positive semi-definite.

First, we consider the case where C' is positive definite. We define the components of some non-zero length vector, x', according to $x' \triangleq [x_0, x_1, x_2, \ldots, x_m]^T$. We also define $x \triangleq [x_0, x_1, x_2, \ldots, x_{m-1}]^T$ to be a subvector containing the first m

19

components of $\boldsymbol{x}'$. Based these definitions, we can write the following:

$$\begin{aligned}
\boldsymbol{x}'^T \boldsymbol{Q} \boldsymbol{x}' &= \boldsymbol{x}'^T (\boldsymbol{C}' + \boldsymbol{\Delta}) \boldsymbol{x}' \\
&= \boldsymbol{x}'^T \boldsymbol{C}' \boldsymbol{x}' + \boldsymbol{x}'^T \boldsymbol{\Delta} \boldsymbol{x}' \\
&= \boldsymbol{x}'^T \boldsymbol{C}' \boldsymbol{x}' + \sum_{i=0}^{m} \sum_{j=0}^{m} x_i \Delta_{i,j} x_j \\
&= \boldsymbol{x}'^T \boldsymbol{C}' \boldsymbol{x}' + 2 x_0 x_m \Delta_{0,m}.
\end{aligned} \tag{2.16}$$

We can eliminate the trivial case where $x_m x_0 = 0$, since it corresponds to $\Delta_{0,m}^U - \Delta_{0,m}^L \to \infty$ which implies that the error is unbounded—a physical impossibility. Setting $\boldsymbol{x}'^T \boldsymbol{Q} \boldsymbol{x}' = 0$ and solving (2.16) for $\Delta_{0,m}$ yields

$$\begin{aligned}
\Delta_{0,m} &= -\frac{\boldsymbol{x}'^T \boldsymbol{C}' \boldsymbol{x}'}{2 x_0 x_m} \\
&= -\frac{1}{2 x_0 x_m} \sum_{i=0}^{m} \sum_{j=0}^{m} x_i c'_{i,j} x_j \\
&= -\frac{1}{2 x_0 x_m} \sum_{i=0}^{m-1} \sum_{j=0}^{m-1} x_i c_{i,j} x_j - \frac{1}{x_0 x_m} \sum_{i=0}^{m-1} x_i c'_{i,m} x_m - \frac{x_m^2 c'_{m,m}}{2 x_0 x_m} \\
&= -\frac{\boldsymbol{x}^T \boldsymbol{C} \boldsymbol{x}}{2 x_0 x_m} - \frac{1}{x_0} \sum_{i=0}^{m-1} x_i c'_{i,m} - \frac{x_m c'_{m,m}}{2 x_0} \\
&= -\frac{\lambda}{2 x_0 x_m} - \frac{1}{x_0} \sum_{i=0}^{m-1} x_i c'_{i,m} - \frac{x_m c'_{m,m}}{2 x_0},
\end{aligned} \tag{2.17}$$

where we have implicitly defined $\lambda = \boldsymbol{x}^T \boldsymbol{C} \boldsymbol{x}$ for an arbitrary choice of $\boldsymbol{x}$, subject to the previously established constraint that $\|\boldsymbol{x}\| > 0$. Before proceeding any further, we will divide this first case into two distinct subcases.

Consider the special subcase where $\boldsymbol{C}'$ is positive definite. For this subcase, we know that $|\Delta_{0,m}| = \left| -\frac{\boldsymbol{x}'^T \boldsymbol{C}' \boldsymbol{x}'}{2 x_0 x_m} \right| > 0$, which precludes the range of $\Delta_{0,m}$ from containing values within some finite interval about $\Delta_{0,m} = 0$. Therefore, a finite upper bound exists on the range of perturbation, $\Delta_{0,m}$, for which $\boldsymbol{Q}$ is positive semi-definite, given that $\boldsymbol{C}'$ is positive definite.

20

For the other subcase C' is not positive definite, but it is still positive semi-definite. For this subcase, we will examine the function $\Delta_{0,m}(x_m)$ under constant x. This function is continuous everywhere except at $x_m = 0$, due to the previously established physical requirement that $x_m x_0 \neq 0$. The first derivative of $\Delta_{0,m}(x_m)$ is given by

$$\frac{\partial \Delta_{0,m}}{\partial x_m} = \frac{\lambda}{2x_0 x_m^2} - \frac{c'_{m,m}}{2x_0}, \tag{2.18}$$

which has exactly two real roots defined by

$$x_m = \pm \left[\frac{\lambda}{c'_{m,m}} \right]^{\frac{1}{2}}, \tag{2.19}$$

corresponding to the critical points of $\Delta_{0,m}(x_m)$. Since C is positive definite, we have that $\lambda > 0$. $c'_{m,m}$ is also positive, since it represents the variance of a random variable. Consider the trivial situation where $c'_{m,m} = 0$. This deterministic constraint would require the last row and column of C' to be all zeros to maintain positive semi-definiteness. Therefore we would also have to constrain $\Delta_{0,m} = 0$ in (2.16) for Q to be positive semi-definite. For all remaining situations, we must have $c'_{m,m} > 0$, since in general, $c'_{m,m}$ represents a nonnegative quantity. Then, for $\lambda > 0$ and $c'_{m,m} > 0$, the function $\Delta_{0,m}(x_m)$ has two real-valued critical points, $x_m^a = -\left[\frac{\lambda}{c'_{m,m}}\right]^{\frac{1}{2}} < 0$ and $x_m^b = \left[\frac{\lambda}{c'_{m,m}}\right]^{\frac{1}{2}} > 0$, on opposite sides of the origin. Next, we examine the second derivative of $\Delta_{0,m}(x_m)$,

$$\frac{\partial^2 \Delta_{0,m}(x_m)}{\partial x_m^2} = \frac{-\lambda}{x_0 x_m^3}, \tag{2.20}$$

which tells us that when $x_0 > 0$, x_m^a corresponds to a local minimum, while x_m^b corresponds to a local maximum. The reverse is true for $x_0 < 0$. This information and the first line of (2.17) tell us that for $x_0 > 0$, we have

$$\Delta_{0,m}(x_m) \geq \Delta_{0,m}(x_m^a) > 0, \forall x_m < 0$$

$$\Delta_{0,m}(x_m) \leq \Delta_{0,m}(x_m^b) < 0, \forall x_m > 0, \tag{2.21}$$

while for $x_0 < 0$, we have

$$\Delta_{0,m}(x_m) \leq \Delta_{0,m}(x_m^a) < 0, \forall x_m < 0$$

$$\Delta_{0,m}(x_m) \geq \Delta_{0,m}(x_m^b) > 0, \forall x_m > 0. \tag{2.22}$$

Then, regardless of the sign on x_0, there exists some interval, $(\Delta_{0,m}^L, \Delta_{0,m}^U)$, for which no combination of $\boldsymbol{x}'$ and $\Delta_{0,m}$ can be found to satisfy $\boldsymbol{x}'^T \boldsymbol{Q} \boldsymbol{x}' = 0$, given the subcase of positive definite $\boldsymbol{C}$ and positive semi-definite $\boldsymbol{C}'$. Therefore, $\boldsymbol{Q}$ is positive semi-definite on some interval, $[\Delta_{0,m}^L, \Delta_{0,m}^U]$, where $\Delta_{0,m}^L < \Delta_{0,m}^U$.

For the second case, we have restricted $\boldsymbol{C}$ to be positive semi-definite, but not positive definite. This means that the least eigenvalue of $\boldsymbol{C}$ is zero [27]. This corresponds to the limiting case where the minimum value of $\lambda \to 0$. The sign of λ is invariant to the scale of $\boldsymbol{x}$. To see this, we substitute $\boldsymbol{x} = a\hat{\boldsymbol{x}}$ and express the sign of λ as

$$\begin{aligned}
\frac{\lambda}{|\lambda|} &= \frac{\boldsymbol{x}^T \boldsymbol{C} \boldsymbol{x}}{|\boldsymbol{x}^T \boldsymbol{C} \boldsymbol{x}|} \\
&= \frac{(a\hat{\boldsymbol{x}})^T \boldsymbol{C}(a\hat{\boldsymbol{x}})}{|(a\hat{\boldsymbol{x}})^T \boldsymbol{C}(a\hat{\boldsymbol{x}})|} \\
&= \frac{a^2 \hat{\boldsymbol{x}}^T \boldsymbol{C} \hat{\boldsymbol{x}}}{|a^2 \hat{\boldsymbol{x}}^T \boldsymbol{C} \hat{\boldsymbol{x}}|} \\
&= \frac{\hat{\boldsymbol{x}}^T \boldsymbol{C} \hat{\boldsymbol{x}}}{|\hat{\boldsymbol{x}}^T \boldsymbol{C} \hat{\boldsymbol{x}}|},
\end{aligned} \tag{2.23}$$

which is clearly unaffected by the sign or magnitude of a ($a > 0$, since we require $\|\boldsymbol{x}\| > 0$). Therefore, we can analyze the sign of λ by restricting $\boldsymbol{x}$ to the set of unit vectors without loss of generality. If we define $\boldsymbol{x} = \hat{\boldsymbol{e}}$, where $\hat{\boldsymbol{e}} = [\hat{e}_0, \hat{e}_1, \hat{e}_2, \ldots, \hat{e}_{m-1}]^T$ is the unit eigenvector corresponding to λ_0, the least eigenvalue of $\boldsymbol{C}$, then $\lambda = \lambda_0$. For $\lambda_0 > 0$, the width of the interval of $\Delta_{0,m}$ for which $\boldsymbol{Q}$ will be positive semi-definite

22

is given by

$$
\begin{aligned}
\Delta^+ &= |\Delta_{0,m}(x_m^b) - \Delta_{0,m}(x_m^a)| \\
&= \left| \left(\frac{[\lambda_0 c'_{m,m}]^{\frac{1}{2}}}{\hat{e}_0} - \frac{1}{\hat{e}_0} \sum_{i=0}^{m-1} \hat{e}_i c'_{i,m} \right) - \left(-\frac{[\lambda_0 c'_{m,m}]^{\frac{1}{2}}}{\hat{e}_0} - \frac{1}{\hat{e}_0} \sum_{i=0}^{m-1} \hat{e}_i c'_{i,m} \right) \right| \\
&= \frac{2[\lambda_0 c'_{m,m}]^{\frac{1}{2}}}{|\hat{e}_0|}.
\end{aligned}
\tag{2.24}
$$

The limit on this expression as $\lambda_0 \to 0$ is $\Delta^+ = 0$. It has already been established that this interval must contain zero. Therefore, as $\lambda_0 \to 0$, C will no longer be positive definite and the only value of $\Delta_{0,m}$ for which Q will be positive semi-definite is $\Delta_{0,m} = 0$, which proves the second case.

2.5.4   Least Upper Bound on Range of Positive Semi-Definiteness.   In Subsection 2.5.3, we derived an expression for Δ^+, an upper bound on the width of the interval for which $\Delta_{0,m}$ will result in a positive semi-definite Q. In this subsection, we will minimize Δ^+ with respect to x' to produce the least upper bound. From this point forward, we will only consider the case of positive definite C, since we have shown that there is zero tolerance for error when C is not positive definite. (2.19) provided us with two optimal choices for x_m which were shown to produce the smallest possible Δ^+ for any given choice of x. Then, the remaining task is to minimize Δ^+ with respect to x.

We start by expanding the expression for Δ^+ from (2.24) and collecting on x_0, writing

$$
\begin{aligned}
\Delta^+ &= \frac{2[\boldsymbol{x}^T \boldsymbol{C} \boldsymbol{x} c'_{m,m}]^{\frac{1}{2}}}{|x_0|} \\
&= \frac{2}{|x_0|} \left[c'_{m,m} \sum_{i=0}^{m-1} \sum_{j=0}^{m-1} x_i x_j c_{i,j} \right]^{\frac{1}{2}} \\
&= \frac{2}{|x_0|} \left[c'_{m,m} \left(\sum_{i=1}^{m-1} \sum_{j=1}^{m-1} x_i x_j c_{i,j} + 2x_0 \sum_{j=1}^{m-1} x_j c_{0,j} + x_0^2 c_{0,0} \right) \right]^{\frac{1}{2}} \\
&= \frac{2}{|x_0|} \left[c'_{m,m} \left(\lambda + 2x_0 \sum_{j=1}^{m-1} x_j c_{0,j} + x_0^2 c_{0,0} \right) \right]^{\frac{1}{2}},
\end{aligned}
\tag{2.25}
$$

where we have reverted back to using $\boldsymbol{x}$ in place of $\hat{\boldsymbol{e}}$, and we have redefined $\lambda \triangleq \sum_{i=1}^{m-1} \sum_{j=1}^{m-1} x_i x_j c_{i,j}$. Next, we examine the function,

$$
f(x_0) = \frac{\lambda + 2x_0 \sum_{j=1}^{m-1} x_j c_{0,j} + x_0^2 c_{0,0}}{x_0^2},
\tag{2.26}
$$

which is defined such that

$$
\Delta^+ = 2[c_{m,m} f(x_0)]^{\frac{1}{2}}
\tag{2.27}
$$

and $f(x_0) > 0$ for positive semi-definite $\boldsymbol{C}$. The first derivative of $f(x_0)$,

$$
\frac{\partial f}{\partial x_0} = -\frac{2\lambda}{x_0^3} - \frac{2}{x_0^2} \sum_{j=1}^{m-1} x_j c_{0,j},
\tag{2.28}
$$

has only one root, given by

$$
x_0^a = \frac{-\lambda}{\sum_{j=1}^{m-1} x_j c_{0,j}}.
\tag{2.29}
$$

The second derivative of $f(x_0)$ is given by

$$
\frac{\partial^2 f}{\partial x_0^2} = \frac{6\lambda}{x_0^4} + \frac{4}{x_0^3} \sum_{j=1}^{m-1} x_j c_{0,j}.
\tag{2.30}
$$

24

When evaluated at the critical point given by (2.29), this expression becomes

$$\frac{\partial^2 f}{\partial x_0^2}\bigg|_{x_0=x_0^a} = \frac{2}{\lambda}\left[\sum_{j=1}^{m-1} x_j c_{0,j}\right]^4 \geq 0, \tag{2.31}$$

which says that x_0^a corresponds to a global minimum whenever $\left|\sum_{j=1}^{m-1} x_j c_{0,j}\right| > 0$. A quick analysis of (2.26) tells us that for $\sum_{j=1}^{m-1} x_j c_{0,j} = 0$, then $f(x_0) = \lambda + c_{0,0}$. Either way, $x_0 = x_0^a$ minimizes $f(x_0)$. Performing this substitution yields the following expressions:

$$\begin{aligned}
f(x_0)|_{x_0=x_0^a} &= \frac{\lambda}{\left[\frac{-\lambda}{\sum_{j=1}^{m-1} x_j c_{0,j}}\right]^2} + \frac{2\sum_{j=1}^{m-1} x_j c_{0,j}}{\frac{-\lambda}{\sum_{j=1}^{m-1} x_j c_{0,j}}} + c_{0,0} \\
&= c_{0,0} - \frac{1}{\lambda}\left[\sum_{j=1}^{m-1} x_j c_{0,j}\right]^2
\end{aligned} \tag{2.32}$$

and

$$\Delta^+ = 2\left[c_{m,m}c_{0,0}\left(1 - \frac{1}{\lambda c_{0,0}}\left[\sum_{j=1}^{m-1} x_j c_{0,j}\right]^2\right)\right]^{\frac{1}{2}}. \tag{2.33}$$

From (2.33), it is apparent that the maximum allowable range of perturbation, Δ^+, will be minimized by maximizing expression,

$$\Upsilon(\tilde{x}) = \frac{1}{\lambda c_{0,0}}\left[\sum_{j=1}^{m-1} x_j c_{0,j}\right]^2, \tag{2.34}$$

where we have defined the $\tilde{x}$ to be a subvector of x, such that $\tilde{x} = [x_1, x_2, x_3, \ldots, x_{m-1}]^T$. Υ_ι is taken to mean the maximum value of $\Upsilon(\tilde{x})$, and is called the statistical degree of information (SDI). Recall that $\lambda = \sum_{i=1}^{m-1}\sum_{j=1}^{m-1} x_i x_j c_{i,j}$, so that $\Upsilon(\tilde{x})$ expands to

$$\Upsilon(\tilde{x}) = \frac{\left(\sum_{j=1}^{m-1} x_j c_{0,j}\right)^2}{c_{0,0}\sum_{i=1}^{m-1}\sum_{j=1}^{m-1} x_i x_j c_{i,j}}. \tag{2.35}$$

Then, maximizing the $\Upsilon(\tilde{\boldsymbol{x}})$, will simultaneously produce the least upper bound on the range of positive semi-definiteness of $\boldsymbol{Q}$.

2.5.5 Existence of the Least Upper Bound.   Next, we will show that a single global maximum exists for $\Upsilon(\tilde{\boldsymbol{x}})$ with respect to each x_k in $\tilde{\boldsymbol{x}}$. Rewriting Υ as a function of a particular x_k, gives us the form

$$
\begin{aligned}
\Upsilon(x_k) =& c_{0,0}^{-1} \left[x_k^2 c_{k,k} + 2x_k \sum_{j=1}^{m-1} (1 - \delta_{j,k}) x_j c_{j,k} + \sum_{i=1}^{m-1} \sum_{j=1}^{m-1} (1 - \delta_{j,k})(1 - \delta_{i,k}) x_i x_j c_{i,j} \right]^{-1} \\
& \times \left[x_k c_{0,k} + \sum_{j=1}^{m-1} (1 - \delta_{j,k}) x_j c_{0,j} \right]^2 \\
=& \left(\frac{c_{0,k}^2}{c_{0,0} c_{k,k}} \right) \frac{g_1(x_k)}{g_2(x_k)},
\end{aligned}
$$

$$(2.36)$$

where

$$
\begin{aligned}
g_1(x_k) =& \left(x_k + \frac{1}{c_{0,k}} \sum_{j=1}^{m-1} (1 - \delta_{j,k}) x_j c_{0,j} \right)^2 \\
g_2(x_k) =& x_k^2 + 2\frac{x_k}{c_{k,k}} \sum_{j=1}^{m-1} (1 - \delta_{j,k}) x_j c_{j,k} + \frac{1}{c_{k,k}} \sum_{i=1}^{m-1} \sum_{j=1}^{m-1} (1 - \delta_{j,k})(1 - \delta_{i,k}) x_i x_j c_{i,j}.
\end{aligned}
$$

$$(2.37)$$

For brevity, we can rewrite g_1 and g_2 as

$$
\begin{aligned}
g_1(x_k) &= (x_k - b_1)^2 \\
g_2(x_k) &= (x_k - b_2)^2 + d^2,
\end{aligned}
$$

$$(2.38)$$

26

where b_1, b_2, and d^2 are given by

$$b_1 = -\frac{1}{c_{0,k}} \sum_{j=1}^{m-1} (1 - \delta_{j,k}) x_j c_{0,j}$$

$$b_2 = -\frac{1}{c_{k,k}} \sum_{j=1}^{m-1} (1 - \delta_{j,k}) x_j c_{j,k} \qquad (2.39)$$

$$d^2 = -b_2^2 + \frac{1}{c_{k,k}} \sum_{i=1}^{m-1} \sum_{j=1}^{m-1} (1 - \delta_{j,k})(1 - \delta_{i,k}) x_i x_j c_{i,j}.$$

From these forms, we recognize g_1 and g_2 to be concave up parabolas, each having a single positive global minimum. We wish to characterize $\Upsilon(x_k)$, which is directly proportional to the ratio of g_1 and g_2 with a positive constant of proportionality. We will consider two cases in analyzing this $\Upsilon(x_k)$.

For the first case, we consider $b_1 = b_2$. According to (2.39), the condition $b_1 = b_2$ would require the trivial solution, $\tilde{x} = 0$, or else $\frac{c_{j,0}}{c_{k,0}} = \frac{c_{j,k}}{c_{k,k}}$ for all integers $j \in [1, m-1]$. The trivial solution is excluded as it presents as a singularity in Υ. The other solution can be interpreted as forcing all columns of, $\widetilde{C}$, the lower-right principal submatrix of C, to be linearly dependent. The implication is that every element in column k of $\widetilde{C}$ would need to be defined as $c_{j,k} = c_{k,k}$. Furthermore, since $\widetilde{C}$ is a covariance matrix, it must be symmetric, forcing $c_{j,j} = c_{k,k}$. This would make every element of $\widetilde{C}$ identical. Because of the dependency between $\{c_{j,0}\}$ and the columns of $\widetilde{C}$, every element of C would also be identical. Therefore C would be positive semi-definite, but not positive definite. From (2.35), we see that this case corresponds to $\Upsilon = 1$, or perfect information. Therefore, Υ is maximized for any choice $\tilde{x}$ whenever $b_1 = b_2$.

For the second case, we consider the imperfect information case, $b_1 \neq b_2$. Since $\lambda > 0$ and $c_{0,0} > 0$, we must also have that $d^2 > 0$. Therefore, $\Upsilon(x_k)$ is strictly nonnegative with no singularities or other discontinuities. Furthermore, an upper bound on the range of $\Upsilon(x_k)$ is $\frac{c_{0,k}^2}{c_{0,0} c_{k,k} d^2}$, and from (2.36) and (2.38), we see that as

27

$x_k \to \pm\infty$, $\Upsilon(x_k) \to \frac{c_{0,k}^2}{c_{0,0}c_{k,k}}$. The first derivative of x_k is given by

$$
\begin{aligned}
\frac{\partial \Upsilon}{\partial x_k} &= \left(\frac{c_{0,k}^2}{c_{0,0}c_{k,k}}\right) \frac{g_2 g_1' - g_1 g_2'}{g_2^2} \\
&= \left(\frac{c_{0,k}^2}{c_{0,0}c_{k,k}}\right) \left(\frac{((x_k - b_2)^2 + d^2)(2)(x_k - b_1)}{((x_k - b_2)^2 + d^2)^2} - \frac{(x_k - b_1)^2(2)(x_k - b_2)}{((x_k - b_2)^2 + d^2)^2}\right) \quad (2.40) \\
&= \left(\frac{2c_{0,k}^2}{c_{0,0}c_{k,k}}\right) \left(\frac{x_k^2(b_1 - b_2) + x_k(b_2^2 - b_1^2 + d^2)}{((x_k - b_2)^2 + d^2)^2} + \frac{b_1^2 b_2 - b_1 b_2^2 - b_1 d^2}{((x_k - b_2)^2 + d^2)^2}\right),
\end{aligned}
$$

which has the two real roots,

$$
\begin{aligned}
x_k &= [2(b_1 - b_2)]^{-1} \left[b_1^2 - b_2^2 - d^2 \pm [(b_1^2 - b_2^2 - d^2)^2 - 4(b_1 - b_2)(b_1^2 b_2 - b_1 b_2^2 - b_1 d^2)]^{\frac{1}{2}}\right] \\
&= [2(b_1 - b_2)]^{-1} \left[b_1^2 - b_2^2 - d^2 \pm [b_1^4 + b_2^4 + d^4 + 6b_1^2 b_2^2 - 4(b_1^3 b_2 + b_1 b_2^3 + b_1 b_2 d^2)\right. \\
&\quad \left. + 2(b_1^2 b_2^2 + b_1^2 d^2 + b_2^2 d^2)]^{\frac{1}{2}}\right] \\
&= \frac{b_1^2 - b_2^2 - d^2 \pm [(b_1 - b_2)^2 + d^2]}{2(b_1 - b_2)} \\
&= \left\{b_1, b_2 - \frac{d^2}{b_1 - b_2}\right\}.
\end{aligned}
$$

$$(2.41)$$

Because $\Upsilon(x_k)$ is continuous and bounded on $(-\infty, \infty)$ and asymptotically approaches unity at either extreme, one of these roots corresponds to a global maximum, while the other corresponds to a global minimum. To determine which critical point corresponds to the maximum, we consider two subcases. In the first subcase, we let $b_1 > b_2$. Then, we have $b_1 > b_2 - \frac{d^2}{b_1 - b_2}$. We will examine the sign of the slope for regions outside of

the interval, $\left[b_2 - \frac{d^2}{b_1-b_2}, b_1\right]$. For $x_k = b_1 + \epsilon$, for any positive ϵ, we have

$$
\begin{aligned}
\frac{\partial \Upsilon}{\partial x_k}\bigg|_{x_k=b_1+\epsilon} &= \left(\frac{2c_{0,k}^2}{c_{0,0}c_{k,k}}\right)\left[(b_1-b_2)^2+d^2\right]^{-2} \times \left[(2b_1\epsilon+\epsilon^2)(b_1-b_2)+\epsilon(b_2^2-b_1^2+d^2)\right] \\
&= \left(\frac{2c_{0,k}^2}{c_{0,0}c_{k,k}}\right)\left[(b_1-b_2)^2+d^2\right]^{-2} \times \left[(b_1^2-2b_1b_2+b_2^2+d^2)\epsilon+(b_1-b_2)\epsilon^2\right] \\
&= \left(\frac{2c_{0,k}^2}{c_{0,0}c_{k,k}}\right)\left[(b_1-b_2)^2+d^2\right]^{-2} \times \left[((b_1-b_2)^2+d^2)\epsilon+(b_1-b_2)\epsilon^2\right] \\
&> 0,
\end{aligned}
$$

$$(2.42)$$

which tells us that $x_k = b_1$ will minimize $\Upsilon(x_k)$, and consequently, that $x_k = b_2 - \frac{d^2}{b_1-b_2}$ will maximize Υ for $b_1 > b_2$. Conversely, when $b_1 < b_2$, we have that $b_1 < b_2 - \frac{d^2}{b_1-b_2}$, so we examine $\frac{\partial \Upsilon}{\partial x_k}$ for $x_k < b_1$. With similarity to (2.43), for $x_k = b_1 - \epsilon$, given any small positive ϵ, we have

$$
\begin{aligned}
\frac{\partial \Upsilon}{\partial x_k}\bigg|_{x_k=b_1-\epsilon} &= \left(\frac{2c_{0,k}^2}{c_{0,0}c_{k,k}}\right)\left[(b_2-b_1)^2+d^2\right]^{-2}\left[-((b_2-b_1)^2+d^2)\epsilon-(b_2-b_1)\epsilon^2\right] \\
&< 0,
\end{aligned}
$$

$$(2.43)$$

which tells us that $x_k = b_1$ will minimize $\Upsilon(x_k)$, and consequently, that $x_k = b_2 - \frac{d^2}{b_1-b_2}$ will maximize Υ for $b_1 < b_2$. Therefore, regardless of which is the greater of b_1 and b_2, $x_k = b_2 - \frac{d^2}{b_1-b_2}$ will maximize $\Upsilon(x_k)$. Since a single computable maximum value exists for $\Upsilon(x_k)$, given any set of elements $\{x_i\}$ from $\tilde{\boldsymbol{x}}$, subject to $i \neq k$, then, a global maximum value also exists for $\Upsilon(\tilde{\boldsymbol{x}})$ for the set of non-zero length sub vectors, $\tilde{\boldsymbol{x}}$. Substituting this global maximum for $\Upsilon(\tilde{\boldsymbol{x}})$ into (2.34) and then into (2.33) is therefore guaranteed to produce the least upper bound, $\Delta_{min}^+ \leq \Delta^+$:

$$\Delta_{min}^+ = 2[c_{0,0}c_{m,m}(1-\Upsilon_\iota)]^{\frac{1}{2}}. \tag{2.44}$$

29

Proof of convergence for an iterative algorithm to find Υ is beyond the scope of this document.

2.5.6 *Upper Bound on the Second-Order Statistical Error of* $p_{\hat{w}_0^\iota|\boldsymbol{w}^\iota}(w_0|\boldsymbol{w}^\iota)$. Without explicitly using our knowledge of $\{c'_{m,0}, c'_{m,1}, c'_{m,2}, \ldots, c'_{m,m-1}\}$, it is impossible to determine the location of the center for the allowable range of $\Delta_{0,m}$. Therefore, we must assume the worst case scenario where $\boldsymbol{C}'$ is not positive definite, and consequently, $\Delta_{0,m}$ must be either strictly nonnegative or strictly nonpositive. In this case, the maximum absolute error in covariance for element $c'_{0,m}$ will be Δ^+_{min}. Rewriting the maximum absolute error in covariance between w_0 and a particular variable, $w_i \notin \mathbb{W}^\iota$, in terms of expected values yields

$$\Delta^+_{i,min} = 2[E[(w_0 - E[w_0])^2]E[(w_i - E[w_i])^2](1 - \Upsilon_\iota)]^{\frac{1}{2}}. \tag{2.45}$$

Using this error bound, the normalized mean squared statistical error of the random estimate (SERE), is given by

$$
\begin{aligned}
\mathcal{E}_\iota &\leq \left[\frac{\sum_{i=0}^M |\Delta^+_{i,min}|^2}{E[(w_0 - E[w_0])^2] \sum_{i=0}^M E[(w_i - E[w_i])^2]} \right]^{\frac{1}{2}} \\
&= \left[\frac{4E[(w_0 - E[w_0])^2] \sum_{i=0}^M E[(w_i - E[w_i])^2](1 - \Upsilon_\iota)}{E[(w_0 - E[w_0])^2] \sum_{i=0}^M E[(w_i - E[w_i])^2]} \right]^{\frac{1}{2}} \\
&= 2[1 - \Upsilon_\iota]^{\frac{1}{2}},
\end{aligned}
\tag{2.46}
$$

which is sufficient to prove the covariance delineation theorem.

2.6 *Experimental Validation of the Covariance Delineation Theorem*

The covariance delineation theorem provides the least upper bound on the statistical error associated with a particular interpolator at any level of recursion. However, since the theorem assumes we have perfect knowledge of the covariance statistics for all random variables under consideration, for the time being, our analysis must be

30

restricted to the first level of recursion. Successive levels would rely on imperfect realizations of random variables, for which the exact covariances are unknown. We shall now consider two possible statistical interpolators. The first is Lane's 4-nearest-neighbors interpolator, which is depicted in Figure 2.1. The second interpolator is

Figure 2.1: 4-Nearest-Neighbors Statistical Interpolator. This figure illustrates the three generations rendered during each level of recursion by the 4-nearest neighbors recursive interpolator. Curved arrows indicate the cycle of generations, while the black arrows indicate which prior data (tails) is used to render additional data (arrowheads). Step 0 represents the initial coarse grid of phase samples.

called the 2-nearest-neighbors interpolator, and is depicted in Figure 2.2. Both interpolators render the first two generations without corrupting the input data that gets used for each new sample that is rendered. Both interpolators rely on statistically imperfect data from prior generation(s) to render the third generation. The key difference between these two interpolators is the first generation. The 4-nearest-neighbors method uses four neighbors each at a relative distance of 1.41 units from the sample being rendered; by contrast, the 2-nearest-neighbors method uses two neighbors each located 1 unit away from the sample being rendered. In the second generation, both interpolators use two neighbors at 1 unit separation, while for the third generation, both interpolators use four neighbors at 1 unit separation. The obvious question con-
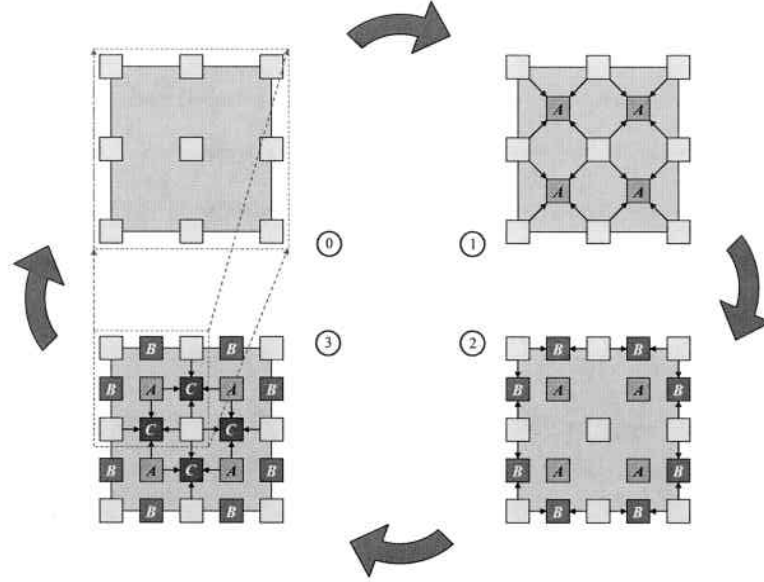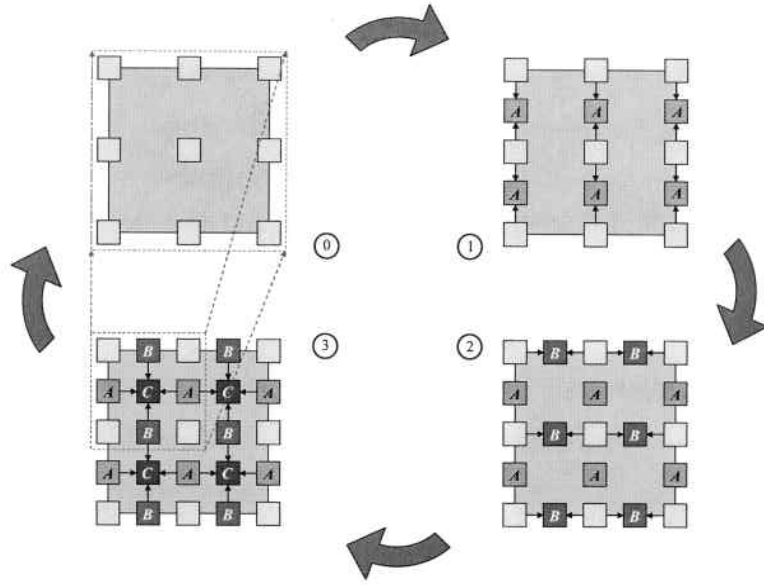
Figure 2.2: 2-Nearest-Neighbors Statistical Interpolator. This figure illustrates the three generations rendered during each level of recursion by the 2-nearest neighbors recursive interpolator, using the same graphical conventions as Figure 2.1

cerning the first generation is whether it is better to use two neighbors within close proximity, or four neighbors that are 40% more distant. (We are also given that both interpolators in this scenario use circularly symmetric inputs.) To answer this question, the first experiment was simulated at various magnitudes of scale with respect to L_0, the outer scale of the atmosphere.

While it is a worthwhile exercise to validate the theorem with the first experiment using only first-level first generation statistics, it is of more practical value to consider an experiment involving phase screens constructed from multiple levels of interpolation. While the stated theorem does not directly apply to such a case, one would intuitively expect that an interpolator with greater accuracy in the first generation of the first level of recursion implies greater statistical accuracy across all levels and generations. This is the focus of the second experiment.

Both experiments were based on the von Kármán spectrum of optical fluctuations. The inner scale was set to zero, and the Rytov approximation for a plane wave in turbulence was applied to obtain the following phase covariance function for

a single layer of turbulence, published in [24]:

$$B_\psi(R_\perp) = 0.033(2\pi)^2 k^2 C_n^2 \Delta z \int\limits_0^\infty \frac{\kappa J_0(\kappa R_\perp)}{\left(\kappa^2 + \frac{4\pi^2}{L_0^2}\right)^{\frac{11}{16}}} d\kappa, \qquad (2.47)$$

where k is the wave number, C_n^2 is the mean refractive index structure constant for the path of turbulence, and Δz is the total path length within turbulence. It is further assumed that C_n^2 varies slowly in the direction of the optical axis. The results published in this chapter have been normalized with respect to L_0, C_n^2, Δz, and wavelength, λ.

2.7 Results

2.7.1 Experiment 1: Single-Level, Single-Generation Interpolation.
For the first experiment, 7.5 million 2x2 phase screens were simulated and statistically interpolated to level 1, generation A for each algorithm. For the 4-nearest-neighbors method, this means using four points to simulate a fourth point at some distance, b, from each of the priors, as depicted in Figure 2.1. For the case of the 2-nearest neighbors method, it means using the leftmost two points of a 2x2 phase screen to simulate a fourth point at a distance of $\frac{b}{\sqrt{2}}$ from the two priors used. See Figure 2.2 for the depiction. SCR is used for both algorithms; the midpoint displacement algorithm is not used in this work.

A maximum likelihood estimator was derived for estimating the covariances between the first interpolated point and the four original points. Figure 2.3 represents the results from this experiment. The figure clearly indicates that the 2-nearest-neighbors interpolator performs considerably better than the 4-point interpolator for the first level and generation. This was predicted by the ordering of the least upper bounds for the statistical error of each interpolator. The 2-point interpolator had a slightly lower upperbound, so we would expect it to perform better than the 4-point interpolator.

33
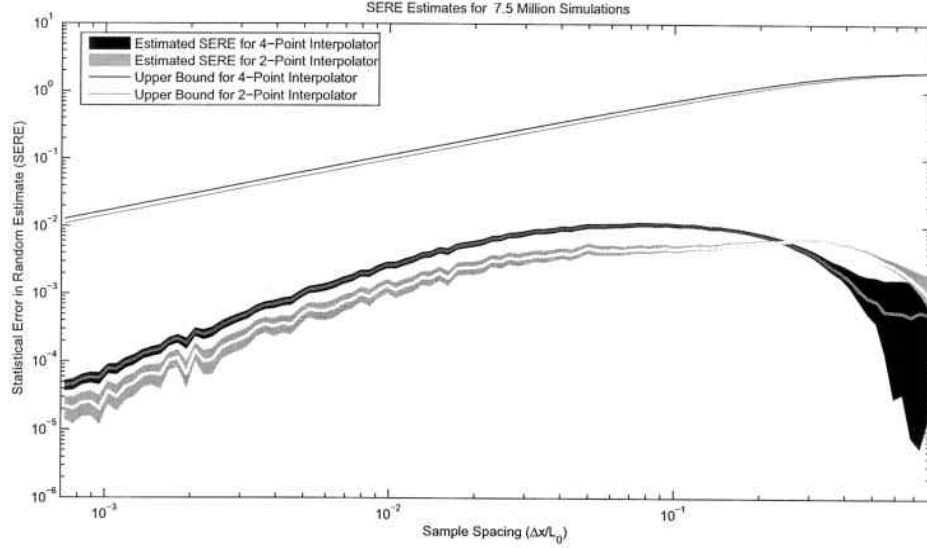
Figure 2.3:   Statistical Error Estimates for Level 1, Generation A. 7.5 Million simulations were performed for each interpolator to obtain maximum-likelihood estimates. Solid regions indicate 99.9% confidence intervals.

2.7.2   Experiment 2: Multilevel Interpolation.   The focus of the second experiment was to test whether the theorem has predictive value in determining which interpolator will perform better across multiple levels of recursion, in the presence of accumulative statistical error. For this experiment, 4.6 million 33x33 phase screens were interpolated from 2x2 phase screens. Figures 2.4–2.6 indicate the same trend that was predicted by the covariance delineation theorem. This initial experiment indicates that the theorem may be extended as a tool for optimizing interpolators across multiple levels of recursion.

2.8   Conclusions

In this chapter, a new approach to statistical interpolation was introduced, based on limited-information successively conditioned rendering (SCR) theory. The resulting algorithm combines the previously published two-step algorithm into a single step algorithm. A new theorem, called the covariance delineation theorem, was introduced as a means for optimizing the statistical accuracy of SCR-based applications, such as statistical interpolation. The theorem was rigorously proven to work for the first-

34
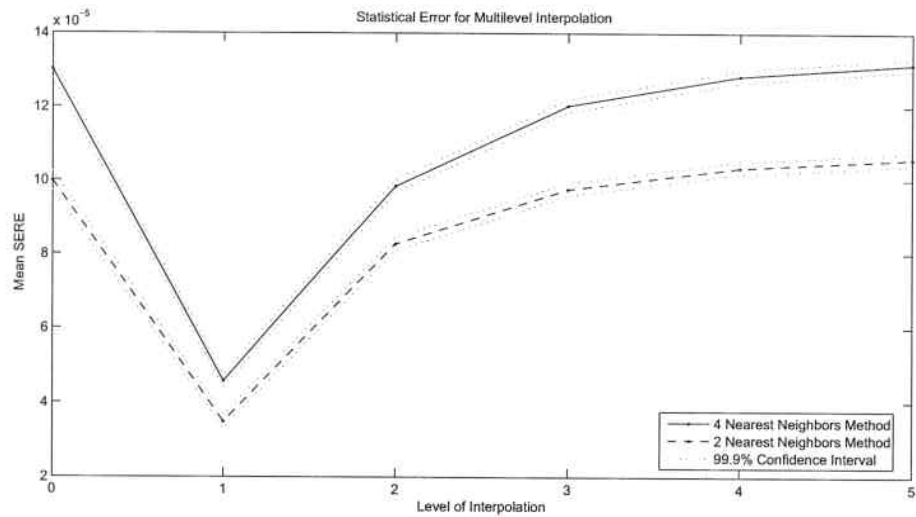
Figure 2.4: Statistical Error Attributed to Each Level. This plot indicates the degree of statistical error per level of statistical interpolation. The data represent 4.6 million phase screen simulations per interpolator. The original phase screens were 2x2, resulting in 33x33 phase screens after 5 levels of recursion. Dotted lines indicate 99.9% confidence intervals.
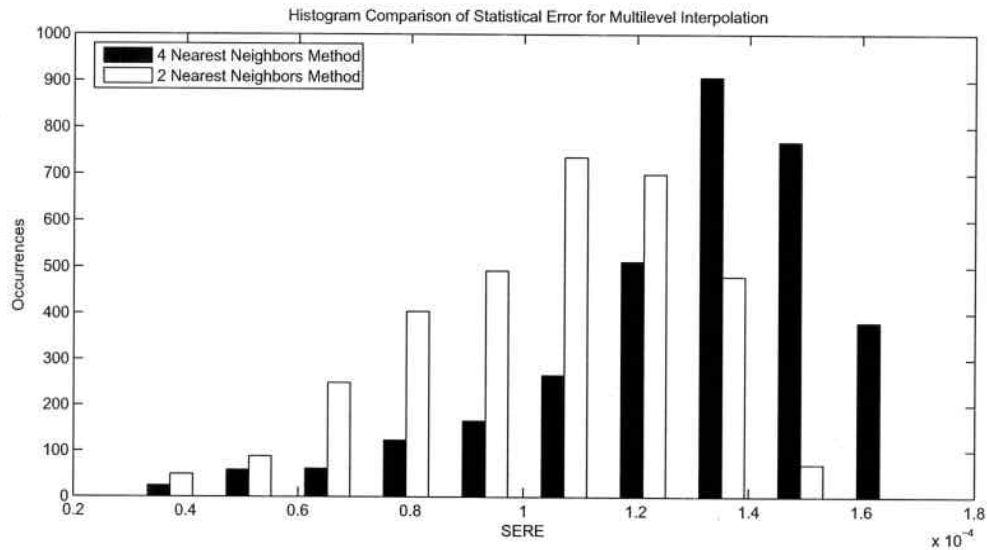
Figure 2.5: Histogram of Multilevel Statistical Error. This histogram compares the distribution of statistical error for each interpolator, without regard to any particular level or generation. The 99.9% confidence interval has a mean width of ±1.56% of the estimated SERE values shown. This histogram reflects the same data shown in Figure 2.4.

level, first generation stage of statistical interpolation. Two different interpolators were tested empirically against the theorem, and the results were consistent with the

35
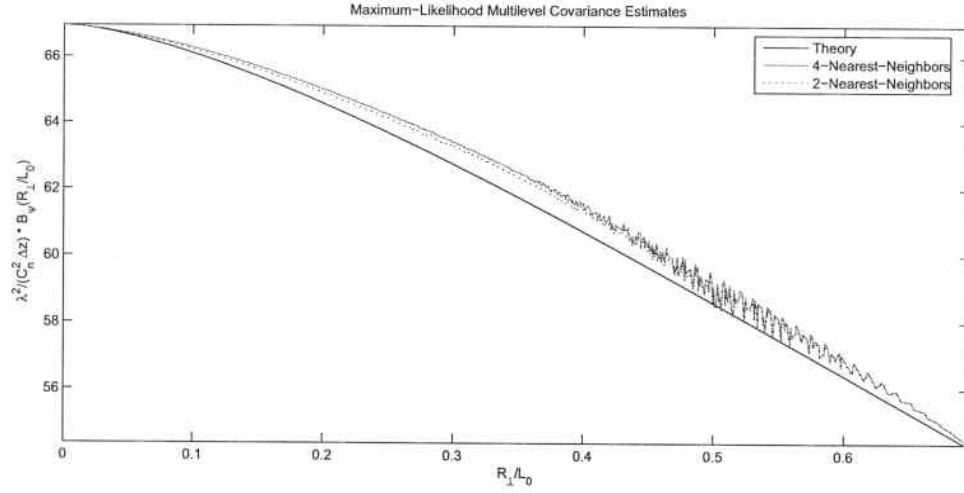
Figure 2.6: Multilevel Phase Covariance Estimates. This plot compares the ideal theoretical phase covariance function to the actual covariance resulting from each interpolator. This plot reflects the same data shown in Figures 2.4 and 2.5.

theory. A second experiment was performed to test the plausible use of the theorem for optimizing statistical interpolation across multiple levels of recursion. The results promising enough to warrant further theoretical study of this problem.

3. A New Approach to Estimating Optical Turbulence Statistics

The effects of optical turbulence have been studied since the early 1960's. [1] Andrews and Phillips, *et al* have published a brief treatise [1] on the matter as it relates to the phenomenon of scintillation, which is complemented by a more complete pedagogical discussion in their classic text, *Laser Beam Propagation Through Random Media* [2]. Nearly all published works on the topic of characterizing optical turbulence rely on three particular underlying assumptions which are all absent from the derivation presented in this chapter. The first assumption is that either strong or weak turbulence conditions apply, requiring two separate analyses of the problem with regard to scattering phenomenology, and hence, scintillation. The second assumption is that the Rytov approximation will lead to sufficiently accurate results. Finally, and perhaps most importantly, the published solutions for Rytov-based scintillation theory all employ the paraxial approximation to optical wave propagation. [2] While there are many other assumptions common to prior works, this work addresses and circumvents each of the aforementioned.

3.1 Roadmap

This chapter begins with a review of prior contributions found in the literature. Next, we provide a mathematical derivation which begins with a model for refractive index fluctuations and ends with a computationally tractable expression for tilt covariance. Section 3.4 gives a description of how the experiment was conducted, what observable data were used and how the data were processed. The section also provides a description of the environmental conditions at the time of the experiment. Results-oriented readers may wish to skip to Sections 3.5 and 3.6 which present and discuss the results from the experiment.

3.2   Background

Several prior works have boasted capability to measure optical turbulence statistics, but all are limited to the three previously stated assumptions. Three statistical parameters traditionally used to characterize turbulence are the refractive index structure constant (C_n^2), the outer scale of turbulence (L_0), and the inner scale of turbulence (l_0). In 1973, Dunphy and Kerr published temporal statistics of C_n^2 for a low-altitude 6 km path, using Kolmogorov-Rytov scintillation theory. [6] In 1979, Valley working in conjunction with the US Air Force published his work on the effects of a non-zero l_0 and finite L_0 on short-term and long-term Strehl ratios. [29] In 1985, Ochs and Hill [21] published early measurements of l_0, using a dual-scintillometer aparatus originally proposed by Livingston. That work was also partially sponsored by the US Air Force. Two years later, Frehlich published the conclusion that a single (paraxial) phase screen does not adequately model inner scale effects on scintillation observations. [10] In 1988, Coulman, *et al* published a method for estimating L_0 using C_n^2 profiles "obtained from spatio-angular correlation measurements of stellar scintillation." [7] The aparatus used is for making those observations is called scintillation detection and ranging (SCIDAR). Hill published another work in 1988 comparing two different scintillation methods for estimating l_0, where the dependence of C_n^2 is cancelled out by taking the ratio of two quantities that are proportionate to C_n^2 and dependent on l_0. [14] Particular advantages were identified for each method. In 1989, Martin and Flatté used a multi-phase screen technique to simulate the scintillation of a spherical wave emanating from within the turbulence, as a means to validate experimentally observed phenomena. [17] The paraxial approximation and Rytov method were employed between each phase screen, and deterministic spatial filters were applied at each screen to allow phase screens of finite extent. In 1992, Hill and Ochs published a work in which micrometeorological measurements of l_0 were in agreement with theory, and scintillation-based estimates of l_0 also agreed fairly well. This work was sponsored in part by the US Army. Hill and Frehlich later published on related work under sponsorship of NASA, NSF, and the US Army, in which they used a

spherical-coordinate scintillation simulation to characterize the relationship between l_0 and irradiance variance under strong turbulence conditions. [15] In the following year, Masciadri and Vernin proposed an angle of arrival technique for estimating l_0 which essentially uses tilt variance estimates made from simultaneous observations through multiple apertures of varying diameters. [18] In 2000, Flatté and Gerber applied multi-phase screen spherical-wave and plane-wave simulations to the Hill spectrum of turbulence and concluded that under strong turbulence conditions their results did not match first order analytical predictions of scintillation. That work was supported in part by the US Navy. [8] In 2002, Whiteley presented an analytical technique for using a multi-aperture or multi-source system to estimate a C_n^2 profile. [32] While the technique is not scintillation-based, the derivation still applies the paraxial assumption and uses the Kolmogorov spectrum. That work was sponsored by the US Air Force. In 2004, Ziad and Schöck, *et al*, compared three astronomical techniques for measuring L_0, including two methods based on the Shack-Hartmann wavefront sensor, and a third interferometric technique. [34] Also in 2004, Cain published a technique under Air Force sponsorship for C_n^2 profile estimation using a wavefront sensing array and a single laser guide star. Most recently, in 2006, Vetelino *et al* published results from a 2005 experiment in which simultaneous estimates of C_n^2, l_0, and L_0 were computed from scintillation observations collected using three separate receiving apertures of different sizes. [30] That work was also partly supported by the US Navy.

In this work, we present an alternative approach to the problem of estimating statistical turbulence parameters. Rytov theory will not be applied, and neither will the paraxial (a.k.a. phase screen) approximation. The technique being explored is unaffected by scintillation, and consequently the effects of atmospheric scattering can be ignored. The technique is similar to the angle of arrival (AA) methods described by Masciadri [18] and Ziad [34], and to the differential tilt-based technique proposed by Whiteley [32], but it is perhaps most closely related to the method proposed by Cain [3], and is in actuality an extension of the same idea. Instead of extracting

a C_n^2 profile from tilt variances estimated over multiple apertures, we are using a single aperture to estimate tilt covariance for multiple pairs incoherent point sources. The estimated tilt covariances which are subsequently applied to estimate the spatial covariance of refractive index fluctuations. Since the resulting system of equations is underdetermined, we constrain the problem by applying a three-parameter von Kármán model with finite outer scale and non-zero inner scale. For this work, we chose a one-dimensional model for the spectrum of refractive index fluctuations, defined under the typical assumptions of homogeneity and isotropy [2].

3.3 Derivation

We define $B_n(R)$ as the refractive index spatial covariance function where we assume that the random refractive index field, $n(\boldsymbol{P})$, is statistically homogenous and isotropic within a plane that is parallel to the tangential plane at the surface of a spherically-modeled earth for the optical path of interest. R refers to the Euclidean distance between two points, while $\boldsymbol{P}$ refers to a point in three-space. We wish to search for some function, $B_n(R)$, which provides the best statistical description of a particular set of Zernike tilt [24] observations.

3.3.1 Tilt Covariance. First, we define the covariance operator as

$$\mathrm{cov}[x,y] \triangleq E[xy] - E[x]E[y], \tag{3.1}$$

and we define *unscaled* Zernike tilt as the quantity,

$$\alpha \triangleq \iint\limits_A \varphi(\boldsymbol{P}_\perp)\boldsymbol{P}_\perp \cdot \hat{\boldsymbol{x}}d\boldsymbol{P}_\perp, \tag{3.2}$$

where $\boldsymbol{P}_\perp$ represents a point in two-space, transverse to the optical (z) axis, and φ represents the optical phase delay between two points in space, separated by distance

40

Δz along the optical axis and by a transverse distance of $|\boldsymbol{P}_\perp(\Delta z) - \boldsymbol{P}_\perp(0)|$:

$$\varphi(\boldsymbol{P}_\perp) \triangleq k \frac{|\boldsymbol{P}(\Delta z) - \boldsymbol{P}(0)|}{\Delta z} \int\limits_0^{\Delta z} n(\boldsymbol{P}(z)) dz. \tag{3.3}$$

It is implied by using rectilinearly integrated phase delays that spatially irradiance fluctuations over the aperture are negligible for the optical system under consideration. For a more detailed analysis of this assumption, see Appendix A. This does not preclude its application to conditions of strong turbulence as defined under the Rytov variance criterion, if the aperture is sufficiently large. Let A represent the aperture, and let the plane of the aperture plane be defined as $z = 0$, while the object plane is defined as $z = \Delta z$. We define $\boldsymbol{P}(z)$ to be a 3D position along some line $\boldsymbol{P}$ as a function of position along the optical axis:

$$\boldsymbol{P}(z) \triangleq \left\langle \frac{z}{\Delta z}(P_{x_1} - P_{x_0}) + P_{x_0}, \frac{z}{\Delta z}(P_{y_1} - P_{y_0}) + P_{y_0}, z \right\rangle, \tag{3.4}$$

and therefore $\boldsymbol{P}_\perp$ is related to $\boldsymbol{P}$ by

$$\boldsymbol{P}_\perp \triangleq \langle P_{x_0}, P_{y_0} \rangle = \langle \boldsymbol{P}(0) \cdot \hat{\boldsymbol{x}}, \boldsymbol{P}(0) \cdot \hat{\boldsymbol{y}} \rangle. \tag{3.5}$$

Explicitly providing an argument, implies the following:

$$\boldsymbol{P}_\perp(z) = \langle \boldsymbol{P}(z) \cdot \hat{\boldsymbol{x}}, \boldsymbol{P}(z) \cdot \hat{\boldsymbol{y}} \rangle. \tag{3.6}$$

It is inferred in the context of this chapter that angle brackets, $\langle$ and $\rangle$, are used to enclose coordinates for a point, rather than to denote a statistical operation.

We declare $B_n(R)$ to be the refractive index covariance function under homogenous and isotropic turbulence conditions. Let $\boldsymbol{P}_1(z_1)$ represent a line passing through some point in the aperture to another point on the object plane, and let $\boldsymbol{P}_2(z_2)$ represent a second line passing through some other point on the aperture to a second point of interest on the object plane. See Figure 3.1. Restrict the choice of $\boldsymbol{P}_1$ and $\boldsymbol{P}_2$, so
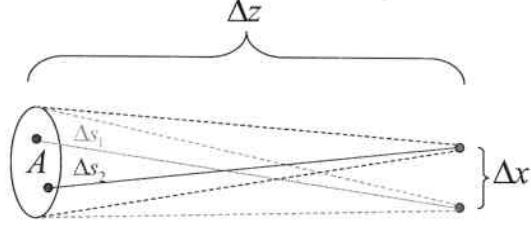
Figure 3.1: Geometry for Tilt Covariance. This figure depicts the geometry for computing tilt covariance for two separate point sources, measured at a common aperture.

that $\boldsymbol{P}_1(\Delta z) = \left\langle -\frac{\Delta x}{2}, 0, \Delta z \right\rangle$ while $\boldsymbol{P}_2(\Delta z) = \left\langle \frac{\Delta x}{2}, 0, \Delta z \right\rangle$. Also, define the following:

$$\Delta s_1 \triangleq |\boldsymbol{P}_1(\Delta z) - \boldsymbol{P}_1(0)|, \tag{3.7}$$

$$\Delta s_2 \triangleq |\boldsymbol{P}_2(\Delta z) - \boldsymbol{P}_2(0)|. \tag{3.8}$$

Using these definitions, we can express the tilt covariance between two points on the object plane separated by Δx along the x-axis:

$$
\begin{aligned}
B_\alpha(\Delta x) =& k^2 \, \mathrm{cov}\left[\left(\iint_A \frac{\Delta s_1}{\Delta z} \int_0^{\Delta z} n(\boldsymbol{P}_1(z_1))dz_1 \times (\boldsymbol{P}_{\perp_1} \cdot \hat{\boldsymbol{x}})d\boldsymbol{P}_{\perp_1} \right), \right. \\
& \left. \left(\iint_A \frac{\Delta s_1}{\Delta z} \int_0^{\Delta z} n(\boldsymbol{P}_2(z_2))dz_2 \times (\boldsymbol{P}_{\perp_2} \cdot \hat{\boldsymbol{x}})d\boldsymbol{P}_{\perp_2} \right) \right] \\
=& \left[\frac{k}{\Delta z}\right]^2 \iint_A \iint_A \Delta s_1 \Delta s_2 \times \int_0^{\Delta z}\int_0^{\Delta z} \mathrm{cov}[n(\boldsymbol{P}_1(z_1)), n(\boldsymbol{P}_2(z_2))] \times dz_1 dz_2 \quad (3.9) \\
& \times (\boldsymbol{P}_{\perp_1} \cdot \hat{\boldsymbol{x}})(\boldsymbol{P}_{\perp_2} \cdot \hat{\boldsymbol{x}})d\boldsymbol{P}_{\perp_1}d\boldsymbol{P}_{\perp_2} \\
=& \left[\frac{k}{\Delta z}\right]^2 \iint_A \iint_A \Delta s_1 \Delta s_2 \times \int_0^{\Delta z}\int_0^{\Delta z} B_n(|\boldsymbol{P}_2 - \boldsymbol{P}_1|)dz_1 dz_2 \\
& \times (\boldsymbol{P}_{\perp_1} \cdot \hat{\boldsymbol{x}})(\boldsymbol{P}_{\perp_2} \cdot \hat{\boldsymbol{x}})d\boldsymbol{P}_{\perp_1}d\boldsymbol{P}_{\perp_2},
\end{aligned}
$$

where we have implied the dependency of B_α on the aperture function, A; the optical path length, Δz; the free-space propagation constant, k; and any parameters which

42

might pertain to the refractive index covariance function B_n. Let us also imply that for a sufficiently long optical path, we may translate $\boldsymbol{P}_1(\Delta z)$ and $\boldsymbol{P}_2(\Delta z)$ by any amount in the $\hat{\boldsymbol{x}}$-direction without affecting $B_\alpha(\Delta x)$, so long as the points are still separated by Δx. That is to say, we assume that tilt is wide-sense stationary in x. Approximating (3.9) for any sizable path by using six nested Riemann sums quickly becomes intractable. The order of difficulty grows proportionately to the square of the propagation length, Δz. In the next subsection we will analyze a more practical numerical approach to the problem.

3.3.2 Step Interpolation. It turns out that a more palatable solution results from substituting numerical integration with a combination of piecewise symbolic integration and interpolation. We begin by defining a sequence of step interpolates, $\{f_i\}$, such that

$$f_i \triangleq B_n(i\Delta R), \tag{3.10}$$

where $0 \leq i \leq N - 2$. Then, we approximate B_n for positive real R, using

$$B_n(R) \approx \sum_{i=0}^{N-2} f_i \, \text{rect}\left(\tfrac{2R}{\Delta R} - (2i+1)\right), \tag{3.11}$$

such that $0 \leq R < (N-1)\Delta R$, and where

$$\text{rect}(x) \triangleq \begin{cases} 1 & i\Delta R \leq x < (i+1)\Delta R \\ 0 & elsewhere \end{cases}. \tag{3.12}$$

After substituting the step-interpolated expression for B_n from (3.11) into the expression for B_α from (3.9), the innermost double integral has a symbolic solution which depends on i, the index of the corresponding interpolate. We define the integral I_i as

$$I_i\left(\boldsymbol{P}_{\perp_1}, \boldsymbol{P}_{\perp_2}, \Delta x\right) \triangleq \int_0^{\Delta z} \int_0^{\Delta z} \text{rect}\left(\tfrac{2R\left(z_1, z_2, \boldsymbol{P}_{\perp_1}, \boldsymbol{P}_{\perp_2}, \Delta x\right)}{\Delta R} - (2i+1)\right) dz_1 dz_2, \tag{3.13}$$

43

so that the innermost double integral from (3.9) becomes

$$
I \triangleq \int\limits_{0}^{\Delta z} \int\limits_{0}^{\Delta z} B_n \left(R \left(z_1, z_2, \boldsymbol{P}_{\perp_1}, \boldsymbol{P}_{\perp_2}, \Delta x \right) \right) dz_1 dz_2
$$

$$
= \sum_{i=0}^{N-2} f_i I_i \left(\boldsymbol{P}_{\perp_1}, \boldsymbol{P}_{\perp_2}, \Delta x \right). \tag{3.14}
$$

Since $\boldsymbol{P}_{\perp_1}$, $\boldsymbol{P}_{\perp_2}$, and Δx, may be held constant with respect to the integration defined in (3.13), we discard them from our notation during this part of the derivation. Earlier, we implicitly defined $R(z_1, z_2)$ to be the Euclidean distance between points $\boldsymbol{P}_1(z_1)$ and $\boldsymbol{P}_2(z_2)$. This quantity is formally defined here as

$$
\begin{aligned}
R(z_1, z_2) \triangleq \big[& (z_1 - z_2)^2 \\
& + [m_{x_1} z_1 + b_{x_1} - (m_{x_2} z_2 + b_{x_2})]^2 \\
& + [m_{y_1} z_1 + b_{y_1} - (m_{y_2} z_2 + b_{y_2})]^2 \big]^{\frac{1}{2}},
\end{aligned} \tag{3.15}
$$

where m_{x_1}, m_{y_1}, m_{x_2}, and m_{y_2} are the respective x-z and y-z slopes for $\boldsymbol{P}_1$ and $\boldsymbol{P}_2$. Similarly, b_{x_1}, b_{y_1}, b_{x_2}, and b_{y_2} are the x and y intercepts at $z = 0$. Since R is a real scalar function, continuously defined over the real z_1-z_2 plane, there is exactly one value from the range of R corresponding to any particular point from the domain of R. Therefore, the locus of points satisfying $R < i\Delta R$ is a subset of the locus of points satisfying $R < (i+1)\Delta R$. We define S_i as the locus of points from $(z_1, z_2) \in [0, \Delta z] \times [0, \Delta z]$ satisfying $R < i\Delta R$. Then, the area of this region, A_i, is defined as

$$
A_i \triangleq \iint\limits_{S_i} dz_1 dz_2. \tag{3.16}
$$

Consequently, we can form the equivalency,

$$
I_i \equiv A_{i+1} - A_i. \tag{3.17}
$$

44

Next, we will solve for A_i analytically. Define the following quantities for substitution:

$$
\begin{aligned}
a_1 &\triangleq 1 + m_{x_1}^2 + m_{y_1}^2, \\
a_2 &\triangleq 1 + m_{x_2}^2 + m_{y_2}^2, \\
a_{12} &\triangleq 2(1 + m_{x_1} m_{x_2} + m_{y_1} m_{y_2}), \\
c_1 &\triangleq 2 \left[m_{x_1} \left(b_{x_1} - b_{x_2} \right) + m_{y_1} \left(b_{y_1} - b_{y_2} \right) \right], \\
c_2 &\triangleq 2 \left[m_{x_2} \left(b_{x_1} - b_{x_2} \right) + m_{y_2} \left(b_{y_1} - b_{y_2} \right) \right], \\
d &\triangleq \left(b_{x_1} - b_{x_2} \right)^2 + \left(b_{y_1} - b_{y_2} \right)^2.
\end{aligned}
\tag{3.18}
$$

Then, rewrite R as

$$
R(z_1, z_2) = [a_1 z_1^2 + z_2 z_2^2 - a_{12} z_1 z_2 + c_1 z_1 - c_2 z_2 + d]^{\frac{1}{2}}.
\tag{3.19}
$$

In order to compute A_i, we must first determine the set of all possible points, $\langle z_1, z_2 \rangle$, such that

$$
0 \le z_1 \le \Delta z
\tag{3.20}
$$

and

$$
0 \le z_2 \le \Delta z
\tag{3.21}
$$

and

$$
a_1 z_1^2 + z_2 z_2^2 - a_{12} z_1 z_2 + c_1 z_1 - c_2 z_2 + d < v,
\tag{3.22}
$$

where

$$
v \triangleq (i \Delta R)^2.
\tag{3.23}
$$

(3.22) comes directly from the inequality, $R < i\Delta R$. Since $a_1 > 0$, we can rewrite the expression from (3.22) as a second-order polynomial in z_1 whose coefficients depend on z_2:

$$
z_1^2 + \left(\frac{c_1 - a_{12} z_2}{a_1} \right) z_1 + \frac{a_2 z_2^2 - c_2 z_2 + d - v}{a_1} < 0.
\tag{3.24}
$$

45

To complete the square, we define b and h such that

$$-h + (z_1 + b)^2$$
$$= z_1^2 + \left(\frac{c_1 - a_{12}z_2}{a1}\right) z_1 + \frac{a_2 z_2^2 - c_2 z_2 + d - v}{a_1}.$$

(3.25)

This leads to the definitions

$$b \triangleq \frac{c_1 - a_{12}z_2}{2a_1}$$
$$h \triangleq \left(\frac{a_{12}^2}{4a_1^2} - \frac{a_2}{a_1}\right) z_2^2 - \left(\frac{a_{12}c_1}{2a_1^2} - \frac{c_2}{a_1}\right) z_2 + \left(\frac{c_1^2}{4a_1^2} - \frac{d-v}{a_1}\right).$$

(3.26)

Since z_1, b, and h are real, (3.22) becomes simply

$$-b - h^{\frac{1}{2}} < z_1 < -b + h^{\frac{1}{2}}.$$

(3.27)

We introduce another set of substitutions that will allow us to cleanly bound z_1 in terms of z_2:

$$q_0 \triangleq \frac{a_{12}}{2a_1},$$

$$q_1 \triangleq \frac{c_1}{2a_1},$$

$$q_2 \triangleq \frac{a_{12}^2}{4a_1^2} - \frac{a_2}{a_1},$$

(3.28)

$$q_3 \triangleq \frac{a_{12}c_1}{2a_1^2} - \frac{c_2}{a_1},$$

$$q_4 \triangleq \frac{c_1^2}{4a_1^2} - \frac{d-v}{a_1}.$$

The resulting upper and lower bounds from (3.27) are

$$-b - h^{\frac{1}{2}} = q_0 z_2 - q_1 - [q_2 z_2^2 - q_3 z_2 + q_4]^{\frac{1}{2}},$$
$$-b + h^{\frac{1}{2}} = q_0 z_2 - q_1 + [q_2 z_2^2 - q_3 z_2 + q_4]^{\frac{1}{2}},$$

(3.29)

which implies that

$$q_2 z_2^2 - q_3 z_2 + q_4 \geq 0.$$

(3.30)

46

We label

$$p(z_2) = q_2 z_2^2 - q_3 z_2 + q_4 \tag{3.31}$$

as the characteristic polynomial for z_2. From (3.18) and (3.28) it is clear that $|q_2| \ll 1$. Therefore, the special case where $q_2 = 0$ must be tested prior to treating (3.31) as quadratic. Next, we will show that $q_2 \leq 0$. Expanding q_2 in terms of its defining slopes, yields

$$
\begin{aligned}
q_2 &= \frac{1}{a_1} \left(\frac{a_{12}^2}{4a_1} - a_2 \right) \\
&= \frac{1}{1+m_{x_1}^2+m_{y_1}^2} \left[\frac{\left(1+m_{x_1}m_{x_2}+m_{y_1}m_{y_2}\right)}{1+m_{x_1}^2+m_{y_1}^2} - \left(1 + m_{x_2}^2 + m_{y_2}^2\right) \right] \\
&= - \frac{\left(m_{x_1}m_{y_2}-m_{y_1}m_{x_2}\right)^2+\left(m_{x_1}-m_{x_2}\right)^2+\left(m_{y_1}-m_{y_2}\right)^2}{1+m_{x_1}^2+m_{y_1}^2}
\end{aligned}
\tag{3.32}
$$

$$\leq 0.$$

This result is important because it allows us to directly use the discriminant corresponding to the characteristic polynomial of z_2 to confine our analysis to cases where the following inequality holds true:

$$q_3^2 \geq 4q_2 q_4. \tag{3.33}$$

All other cases are not physically realizable.

The next step in computing A_i is to identify the allowable interval for z_2. Since $q_2 \leq 0$, the characteristic polynomial for z_2 is concave down. For cases where (3.33) is true, we can say that there is exactly one or zero such intervals on z_2 contributing to A_i satisfying both (3.30) and (3.21). We label the upper and lower bounds of this interval, ζ_2^- and ζ_2^+, respectively. If for the particular case of interest there are no such intervals, then $A_i = 0$. We continue our analysis, assuming that the interval $[\zeta^-, \zeta^+]$ exists for the given choice of i.

It may be necessary to partition $[\zeta_2^-, \zeta_2^+]$ into multiple mutually exclusive subintervals for which the limits on z_1 satisfying (3.20) and (3.22) are fixed. In other words,

47

the limits of integration for z_1 may change, depending on the value of z_2. We rewrite (3.16) to reflect the use of such partitions:

$$A_i = \beta_1 \int\limits_{\Sigma_1} \int\limits_0^{\Delta z} dz_1 dz_2 + \beta_2 \int\limits_{\Sigma_2} \int\limits_0^{-b+\sqrt{h}} dz_1 dz_2 + \beta_3 \int\limits_{\Sigma_3} \int\limits_{-b-\sqrt{h}}^{\Delta z} dz_1 dz_2 + \beta_4 \int\limits_{\Sigma_4} \int\limits_{-b-\sqrt{h}}^{-b+\sqrt{h}} dz_1 dz_2$$

$$= \beta_1 \Delta \Sigma_1 \Delta z + \beta_2 \int\limits_{\Sigma_2} (-b + h^{\frac{1}{2}}) dz_2 + \beta_3 \Delta z + \beta_3 \int\limits_{\Sigma_3} (b + h^{\frac{1}{2}}) dz_2 + 2\beta_4 \int\limits_{\Sigma_4} h^{\frac{1}{2}} dz_2,$$

$$(3.34)$$

where $\Delta \Sigma_1 \triangleq \int_{\Sigma_1} dz_2$. A boolean ($\beta$) coefficient is placed before each of the integrals corresponding to the four possible partitions. Each β coefficient is restricted to have a value of either 1 or 0. We will reduce (3.34) by defining the definite integrals:

$$Q_b(\varsigma_2^-, \varsigma_2^+) \triangleq \int\limits_{\varsigma_2^-}^{\varsigma_2^+} b dz_2$$

$$= \int\limits_{\varsigma_2^-}^{\varsigma_2^+} [q_1 - q_0 z_2] dz_2 \qquad (3.35)$$

$$= \left[q_1 z_2 - \frac{q_0 z_2^2}{2} \right]_{\varsigma_2^-}^{\varsigma_2^+}$$

and

$$Q_h(\varsigma_2^-, \varsigma_2^+) \triangleq \int\limits_{\varsigma_2^-}^{\varsigma_2^+} h^{\frac{1}{2}} dz_2$$

$$= \int\limits_{\varsigma_2^-}^{\varsigma_2^+} \left[q_2 z_2^2 - q_3 z_2 + q_4 \right]^{\frac{1}{2}} dz_2. \qquad (3.36)$$

48

If we presume that $q_2 = 0$, then (3.36) evaluates to [33]

$$Q_h = \int_{\varsigma_2^-}^{\varsigma_2^+} [q_3 z_2 + q_4]^{\frac{1}{2}} dz_2$$

$$= \left[\frac{2(q_4 + q_3 z_2)^{\frac{3}{2}}}{3 q_3} \right]_{\varsigma_2^-}^{\varsigma_2^+} .$$

(3.37)

Otherwise, for $q_2 < 0$, we have [33]

$$Q_h = \left[[q_2 z_2^2 - q_3 z_2 + q_4]^{\frac{1}{2}} \left(\frac{z_2}{2} - \frac{q_3}{4 q_2} \right) \right.$$

$$\left. - \frac{4 q_2 q_4 - q_3^2}{8 q_2^{\frac{3}{2}}} \ln \left\{ 2 q_2^{\frac{1}{2}} z_2 - q_3 q_2^{-\frac{1}{2}} + 2[q_2 z_2^2 - q_3 z_2 + q_4]^{\frac{1}{2}} \right\} \right]_{\varsigma_2^-}^{\varsigma_2^+}$$

(3.38)

Since the integrand is known to be real over the entire interval of integration, we can safely analyze just the real part. This is computationally more efficient because $Q_h(0, \varsigma_2^-)$ and $Q_h(0, \varsigma_2^+)$ are complex conjugates. The resulting expression is

$$Q_h = \left[[q_2 z_2^2 - q_3 z_2 + q_4]^{\frac{1}{2}} \left(\frac{z_2}{2} - \frac{q_3}{4 q_2} \right) - \frac{4 q_2 q_4 - q_3^2}{8 q_2^{\frac{3}{2}}} \right.$$

$$\left. \times \arctan \left\{ \frac{2 |q_2|^{\frac{1}{2}} z_2 + q_3 |q_2|^{-\frac{1}{2}}}{2[q_2 z_2^2 - q_3 z_2 + q_4]^{\frac{1}{2}}} \right\} \right]_{\varsigma_2^-}^{\varsigma_2^+} .$$

(3.39)

Using these integral function definitions, we rewrite (3.34) as

$$A_i = \beta_1 \Delta \Sigma_1 \Delta z + \beta_2 [-Q_b(\Sigma_2) + Q_h(\Sigma_2)]$$

$$+ \beta_3 [\Delta z + Q_b(\Sigma_3) + Q_h(\Sigma_3)]$$

$$+ 2 \beta_4 Q_h(\Sigma_4).$$

(3.40)

The mechanical details on how to solve for the exact boundaries of the z_2 partitions, Σ_1–Σ_4, are beyond the scope of this document. Suffice it to say that each of the par-

49

tition boundaries has an analytical solution whose resulting form may be determined by evaluating a set of test conditions in a particular order.

At this point, we rewrite (3.9) as

$$B_\alpha(\Delta x) = \left[\frac{k}{\Delta z}\right] \iint_A \iint_A \Delta s_1 \Delta s_2 \sum_{i=0}^{N-2} f_i(A_{i+1} - A_i) (\mathbf{P}_{\perp_1} \cdot \hat{\mathbf{x}}) (\mathbf{P}_{\perp_2} \cdot \hat{\mathbf{x}}) \, d\mathbf{P}_{\perp_1} d\mathbf{P}_{\perp_2},$$

(3.41)

and observe that the two innermost integrals from (3.9) have been condensed into a single sum rather than into two nested Riemann sums. Furthermore, the number of elements in this sum can remain fixed with respect to the optical path length, Δz, without further loss of fidelity. Instead, the complexity of this summation depends on the values of l_0 and L_0. To see why this is true, we observe from (3.11) that for $R > (N-1)\Delta R$, B_n is approximated as zero. $(N-1)\Delta R$ should be set to a value greater than or equal to L_0. Additionally, the resolution of B_n is limited to the sample spacing, ΔR. The exact value used for ΔR should be chosen based on l_0. Neither of these quantities depends on path length or geometry. Once ΔR and N are fixed, it is possible to tabulate $B_\alpha(\Delta x)$ for any given path and imaging system and for a desired set of point separations, $\{\Delta x_i\}$.

3.3.3 Spectral Decomposition of Refractive Index Covariance Function.

While the previous expression for tilt covariance in (3.41) may have some utility in determining the characteristic parameters of a particular refractive index covariance function, the results may be limited to a particular set of atmospheric conditions, and to a particular path of observation. In this section, we will derive an efficient means of spectral tabulation that facilitates fast computation of tilt covariance for infinitely many refractive index covariance functions. The traditional starting point for statistical analysis of refractive index fluctuations is in the spectral domain. In this derivation, we conversely start in the spatial domain, since our observable data (tilt covariance) are most closely related to that domain.

50

A complex-valued discrete signal, x, is related to its discrete spectrum, X, by the following pair of relationships: [19]

$$X_{k_2} \triangleq \sum_{k_1=1}^{N_s} x_{k_1} \exp\left\{-j\frac{2\pi}{N_s}(k_1-1)(k_2-1)\right\} \tag{3.42}$$

and

$$x_{k_1} \triangleq \frac{1}{N_s} \sum_{k_2=1}^{N_s} X_{k_2} \exp\left\{j\frac{2\pi}{N_s}(k_1-1)(k_2-1)\right\}. \tag{3.43}$$

In order to take advantage of the discrete Fourier transform (DFT) relationship, we must somehow sample our continuous representation of B_n. One trivial approach is to apply a uniform sampling grid with samples spaced at ΔR. However, this does not bode well with cases where $l_0 \ll L_0$, and such cases are expected to be the norm. We explore an alternative, where we can reduce the total number of samples, N_s. This is accomplished by transforming the R-axis prior to applying a uniform sampling grid and executing the DFT. For that purpose, we define a function, $g(\cdot)$, and its inverse, $g^{-1}(\cdot)$, such that our original spatial variable, R, is transformed into R_g:

$$\begin{aligned} R_g &= g(R), \\ R &= g^{-1}(R_g), \end{aligned} \tag{3.44}$$

We require that $g(\cdot)$ be monotonically increasing. Within the g-transformed space, R_g, we define the uniform sampling distance to be ΔR_g. For this particular problem, we select $g(\cdot)$ using the following criteria:

$$\begin{aligned} g(0) &= 0, \\ g(L_{0_{\max}}) &= L_{0_{\max}}, \end{aligned} \tag{3.45}$$

and

$$\left| B_n(g^{-1}(k_1 \Delta R_g)) - B_n(g^{-1}((k_1-1)\Delta R_g)) \right| \approx K, \tag{3.46}$$

51

where $L_{0_{max}}$ is the maximum outer scale that can be modeled by the resulting spectral decomposition. The third criterion ensures that each transformed sample interval represents approximately equal change in the value of $B_n(R)$. This criterion allows us to efficiently sample a refractive index covariance function with near-zero inner scale without significant aliasing. In order to solve for $g(\cdot)$ we need to assume some initial form for B_n. For this work, we have chosen to use B_n resulting from the von Kármán spectrum with $l_0 = 0$. It can be empirically demonstrated that the von Kármán refractive index covariance function can be closely approximated by

$$B_{n_{vk_0}}(R) \approx C_n^2 L_0^{0.6677} f_n\left(\frac{R}{L_0}\right), \tag{3.47}$$

for $0 \leq R < \infty$ and $l_0 = 0$, where

$$f_n(R) = \frac{2.8835}{(R^{0.7023} + 2.1495 R^{1.6357} + 1.2355)^{5.01}}. \tag{3.48}$$

Once $g(\cdot)$ has been determined, we can construct the transformed spectral basis set. We will use linear interpolation to define the spectral basis continuously in R, in relation to the discrete representation in the transformed space, $\dot{R}_g$. For a particular value of $R : 0 \leq R < L_{0_{max}}$, we define the nearest neighboring samples corresponding to the transformed space as R_a and R_b:

$$
\begin{aligned}
R_a &= g^{-1}\left(\left\lfloor \left| \frac{g(R)}{\Delta R_g} \right| \right\rfloor \Delta R_g\right) \\
R_b &= g^{-1}\left(\left\lceil \left| \frac{g(R)}{\Delta R_g} \right| \right\rceil \Delta R_g\right).
\end{aligned}
\tag{3.49}
$$

Relating (3.49) and the complex exponentials of (3.43), we define the following angular quantities of substitution:

$$
\begin{aligned}
\omega_a &\triangleq \tfrac{2\pi}{N_s}(k_1 - 1)(k_2 - 1) \\
&= \tfrac{2\pi g(R_a)}{N_s \Delta R_g}(k_2 - 1), \\
\omega_b &\triangleq \tfrac{2\pi}{N_s}(k_1)(k_2 - 1) \\
&= \tfrac{2\pi g(R_b)}{N_s \Delta R_g}(k_2 - 1),
\end{aligned}
\tag{3.50}
$$

where we have implied $(k_1 - 1)\Delta R_g \equiv R_a$ and $k_1 \Delta R_g \equiv R_b$, such that k_1 is dependant on R by (3.49). These assignments provide for the following continuous definitions for linearly interpolated real and imaginary spectral basis functions used to decompose $B_n(R)$:

$$
\begin{aligned}
W_{\Re_{k_2}}(R) &= \tfrac{1}{N_s}\left[\tfrac{R - R_a}{R_b - R_a}\left(\cos(\omega_a) - \cos(\omega_b)\right) + \cos(\omega_a)\right], \\
W_{\Im_{k_2}}(R) &= -\tfrac{1}{N_s}\left[\tfrac{R - R_a}{R_b - R_a}\left(\sin(\omega_a) - \sin(\omega_b)\right) + \sin(\omega_a)\right].
\end{aligned}
\tag{3.51}
$$

The bases in (3.51) come directly from applying (3.50) to (3.43). $W_{\Re_{k_2}}(R)$ is the real component of the k_2^{th} spectral basis function, and $W_{\Im_{k_2}}(R)$ is the corresponding imaginary component. According to these definitions, the continuous function $B_n(R)$ may be approximately reconstructed using the spectral decomposition,

$$
\begin{aligned}
\hat{B}_n(R) &\triangleq \sum_{k_2=1}^{N} \left(\Re\left\{\Phi_{n_{k_2}}\right\} W_{\Re_{k_2}}(R) + \Im\left\{\Phi_{n_{k_2}}\right\} W_{\Im_{k_2}}(R) \right) \\
&\approx B_n(R),
\end{aligned}
\tag{3.52}
$$

where the k_2^{th} complex spectral component is defined from (3.42) as

$$
\Phi_{n_{k_2}} \triangleq \sum_{k_1=1}^{N_s} B_n\left(g^{-1}((k_1 - 1)\Delta R_g)\right) \exp\left\{-j\tfrac{2\pi}{N_s}(k_1 - 1)(k_2 - 1)\right\}.
\tag{3.53}
$$

By applying (3.41) to each of the N_s real and imaginary spectral basis functions defined in (3.51), a table can be generated for $B_\alpha(\Delta x)$ which can be used on any form

of $B_n(R)$, in the following manner:

$$B_\alpha(\Delta x) = \sum_{k_2=1}^{N_s} \left(B_{\alpha,k_2,\Re}(\Delta x)\Re\left\{\Phi_{n_{k_2}}\right\} + B_{\alpha,k_2,\Im}(\Delta x)\Im\left\{\Phi_{n_{k_2}}\right\} \right). \tag{3.54}$$

$B_{\alpha,k_2,\Re}(\Delta x)$ and $B_{\alpha,k_2,\Im}(\Delta x)$ are the tabulated tilt covariance values associated with a source separation of Δx and the k_2^{th} real and imaginary spectral bases.

3.3.4 3-Parameter von Kármán Model for B_n. Next, we introduce an efficient method for tabulating the refractive index covariance function associated with the von Kármán spectrum. The von Kármán spectrum for refractive index fluctuations is given by [2]

$$\Phi_{n_{vk}}(\kappa) = 0.033 C_n^2 \left[\kappa^2 + \left(\tfrac{2\pi}{L_0}\right)^2\right]^{-\frac{11}{6}} \exp\left\{-0.02853\kappa^2 l_0^2\right\}, \tag{3.55}$$

where the κ denotes one-dimensional spatial frequency. $B_n(R)$ and $\Phi_n(\kappa)$ are related by [2]

$$B_n(R) \equiv \frac{4\pi}{R} \int_0^\infty \Phi_n(\kappa) \sin(\kappa R)\kappa d\kappa. \tag{3.56}$$

It can be empirically shown that the von Kármán model very nearly obeys the following compound scaling property:

$$B_{n_{vk}}(C_n^2, l_0, L_0, R) \approx C_n^2 L_0^{0.6677} B_{n_{vk}}\left(1, \tfrac{l_0}{L_0}, 1, \tfrac{R}{L_0}\right) \tag{3.57}$$

This property allows us to tabulate B_n as a function of only R and l_0. For our purposes, we used a 1000-point log-spaced sampling grid in R and a 101-point uniform grid for $\frac{l_0}{L_0} \in [0, 0.01]$. Linear interpolation is used to obtain B_n for other combinations of R and l_0. This approach is fast and convenient. (3.57) is a valid approximation for values of L_0 on the interval $[1, 100]$. For this work, units of meters were applied to all spatial quantities.

54

3.4 Experiment

We designed a simple experiment to demonstrate how a simple low-cost apparatus can be deployed to make field measurements of the refractive index spatial covariance function, B_n.

3.4.1 Description. The imaging system consisted of a Photometrics®512B high-speed broadband CCD camera [26], coupled to a Meade®8-in LX200GPS Scmidt-Cassegrain telescope [20]. The LX200GPS has a 2 m focal length, and was custom-fitted with a 4 cm circular aperture stop. Camera specifications include a 512 x 512 detector array of 16 μm x 16 μm broadband pixels. Peak pixel quantum efficiency is achieved at a wavelength of approximately 575 nm, with quantum efficiency ranging $0.90 < \eta < 0.93$, for $500\,\text{nm} < \lambda < 675\,\text{nm}$. A 532 nm narrowband filter was placed directly over the aperture stop to reduce the photon flux at the receiver. The camera transmits uncompressed image data to a PC via a PCI card at a rate of 28 fps. A photograph of this apparatus is shown in Figure 3.2.

The imaging apparatus was configured to view a passive array of extended sources through a 100 m atmospheric path at 1.25 m above ground. The source array was configured to be one dimensional, parallel to the ground, and perpendicular to the optical axis. Figure 3.3 shows the pattern for the source array. The distribution of sources was stochastically optimized to achieve the maximum number of distinct separation distances between source pairs that are uniformly-distributed over 22.5 cm. Table 3.1 gives the relative positions of each source, while Figure 3.4 shows thirty-three corresponding usable distances that follow a nearly-uniform distribution. The reason for favoring a uniform distribution of source-pair distances is that the distribution of relevant information with respect to Δx is unknown. Therefore, this is the distribution which will most likely maximize the total information content in the data collected. Likewise, the reason for maximizing the number of distinct source-pair distances is also to maximize the total amount of useful information recorded. The span of 22.5 cm is designed to nearly fill the field of view for an optical path length (OPL) of 100 m,

Figure 3.2:   Imaging Apparatus. This figure shows the setup for the imaging apparatus used in the experiment.

while still allowing some room for relative motion between the sources and the imaging instrument.

3.4.2 Observables.   In order to account for such relative platform motion, the observed tilt covariance, $B_{\tilde{\alpha}}$, is defined as

$$B_{\tilde{\alpha}} \triangleq \text{cov}[\tilde{\alpha}_1, \tilde{\alpha}_2], \tag{3.58}$$

where,

$$\begin{aligned} \tilde{\alpha}_1 &\triangleq \alpha_1 + \alpha_\eta \\ \tilde{\alpha}_2 &\triangleq \alpha_2 + \alpha_\eta. \end{aligned} \tag{3.59}$$
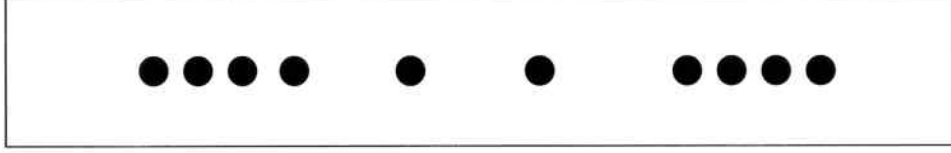
56

Figure 3.3: Passive Source Array. This figure shows pattern used for the source array. There are ten sources placed in a manner which gives thirty-three uniformly-distributed distances of separation.

Table 3.1: Relative Source Positions

Source	Position (cm)
1	0.0000
2	1.5000
3	3.0000
4	4.7539
5	8.6730
6	13.0252
7	18.0000
8	19.5000
9	20.1000
10	22.5000

Consequently,

$$B_{\tilde{\alpha}} = B_{\alpha} + \text{var}[\alpha_{\eta}], \tag{3.60}$$

where α_{η} is the noise in tilt due to translational platform motion. The platform motion is assumed to be statistically independent from atmospheric tilt. Pitch and roll do not affect the observations, and yaw is assumed to be negligible. $\text{var}[\alpha_{\eta}]$ is a fourth unwanted parameter that will be estimated along with the other turbulence parameters. The random platform motion, α_{η}, is constant with respect to source position for simultaneous observations: $\alpha_{\eta} = \alpha_{\eta}(x_1) \equiv \alpha_{\eta}(x_2)$.

Next, we address spatial aliasing of the system. Using Nyquist theory, the aliasing criterion for this system is $\Delta_{pix} \leq \frac{\lambda f}{4D}$. We get this relationship from the fact that the maximum spatial frequency of the electromagnetic (EM) field at the detector is $\frac{\lambda f}{D}$ [11]. The intensity pattern has twice the maximum spatial frequency as the EM field, and Nyquist sampling requires the maximum sampling distance to be twice the maximum frequency of the intensity pattern. For our particular imaging system, we
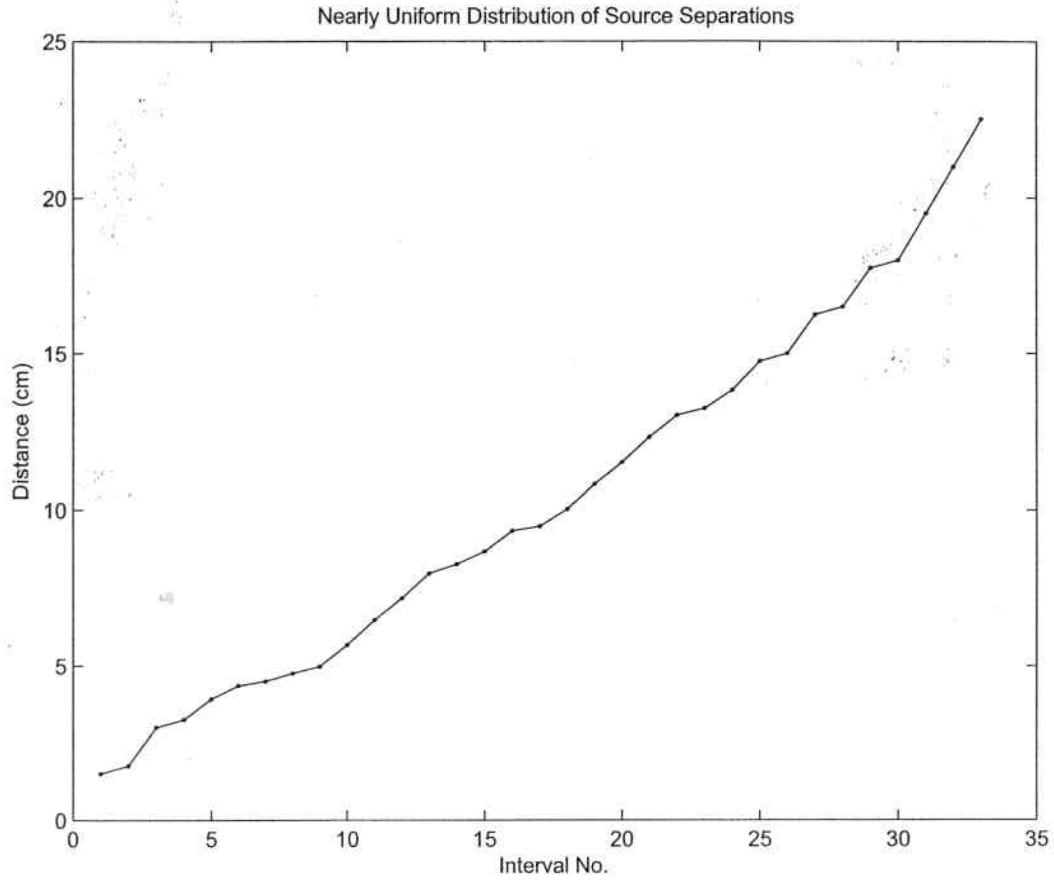
57

Figure 3.4: Distribution of Source Separations. This plot displays the distribution of distances between pairs of sources. from Figure 3.3. The distances are stochastically optimized to be maximal in number and nearly uniform in distribution.

would need a pixel pitch of $\Delta_{pix} \leq 6.65\ \mu$m to eliminate all aliasing. Our design is therefore subject to some aliasing. However, the spatial frequency power spectrum tapers off linearly, since it is scaled by the autocorrelation of the pupil function. Using this analysis, we can directly compute the maximum total power of aliasing, as a fraction of the maximum total spatial power in the image. The maximum spatial image power is proportionate to

$$K_{\max} \propto \frac{\pi}{3\Delta_{nyq}^2},\qquad (3.61)$$

58

where Δ_{nyq} is the maximum pixel pitch allowed by the Nyquist criterion. This definition comes directly from using the formula for the volume of a right-circular cone [28]. The amount of non-aliased spatial image power for the image system we used is proportionate to

$$K_{pix} \propto \frac{\pi \Delta_{nyq}}{3\Delta_{pix}^3} + \left(1 - \frac{\Delta_{nyq}}{\Delta_{pix}}\right)\frac{\pi}{\Delta_{pix}^2}, \qquad (3.62)$$

which comes from computing the volume of the same cone, intersected with a right-circular cylinder. The resulting ratio of aliased spatial power to total spatial image power is given by

$$\begin{aligned} \mathcal{S} &\triangleq 1 - \frac{K_{pix}}{K_{\max}} \\ &= 1 - \left(\frac{\Delta_{nyq}}{\Delta_{pix}}\right)^2 \left[3 - 2\frac{\Delta_{nyq}}{\Delta_{pix}}\right]. \end{aligned} \qquad (3.63)$$

For our particular instrument, the fraction of aliased power for the worst-case image scenario is $\mathcal{S} = 0.6254$. Because this is quite poor, we selected rather large (1 cm) diameter sources. The extended sources enable us to more accurately estimate tilt because they produce images with lower overall spatial frequency content, while simultaneously improving the signal-to-noise ratio (SNR) of the system. We purposely did not further reduce the aperture of the system to avoid all aliasing. Doing so would have degraded the resolving power of the imaging system. This would have required larger, and hence fewer sources, due to optical turbulence effects. As the aperture becomes smaller, the potential for scintillation to occur is greater. Using a larger, slightly aliased aperture allows us to use less robust image processing techniques that do not need to account for scintillation. Alternatively, we could have selected a different camera with smaller pixels. However, this would require lengthening the exposure time, in order to achieve sufficient photon flux. This is may not be desirable because the atmosphere is continually changing. Short exposure times allow us to assume the atmosphere is frozen during the integration period for each frame. While our system is not parametrically optimized, it is a sufficient prototype for making measurements of tilt.

The image processing algorithm to extract tilt observations from a sequence of images is straightforward. First, the horizontal and vertical profiles are computed for each frame, by summing all of the columns and then all of the rows. Then, peaks are detected from the horizontal profile, detecting the horizontal location of each source image. Next, the vertical location of the row of sources is detected from the horizontal profile. At this point, a small square mask is used to extract an isolated image of each source. The centroid is computed for each source, as a preliminary estimate for the source's location. Then, each source is extracted once more from the original image, using a new square, centered at the centroid. Next, a horizontal profile is computed for each source image. Each profile is interpolated by a factor of ten, before it is correlated with a truncated normal probability density function (pdf). The peak correlation is used as the subpixel estimate for the location of the image source. Now, we will show that the resulting quantity is proportionate to tilt if momentarily neglect the noise component.

Consider the diagram in Figure 3.5, which relates angle of arrival to diffraction-less image displacement, as predicted by free-space geometric optics. We will assume that the refractive index is constant with respect to wavelength, for all media under consideration. Geometric tilt, α_g, is closely related to the angle of arrival, θ. For our application, we have the condition, $|\Delta x_i| \ll |f|$, which leads to the approximation, $\sin(\theta) = \frac{\Delta x_i}{f} \approx \theta$. We formally define geometric tilt as the optical phase delay per unit distance across the aperture in the $\hat{x}$-direction:

$$
\begin{aligned}
\alpha_g &\triangleq \frac{2\pi \Delta x_i}{\lambda f} \\
&= k \frac{\Delta x_i}{f} \\
&= k\theta,
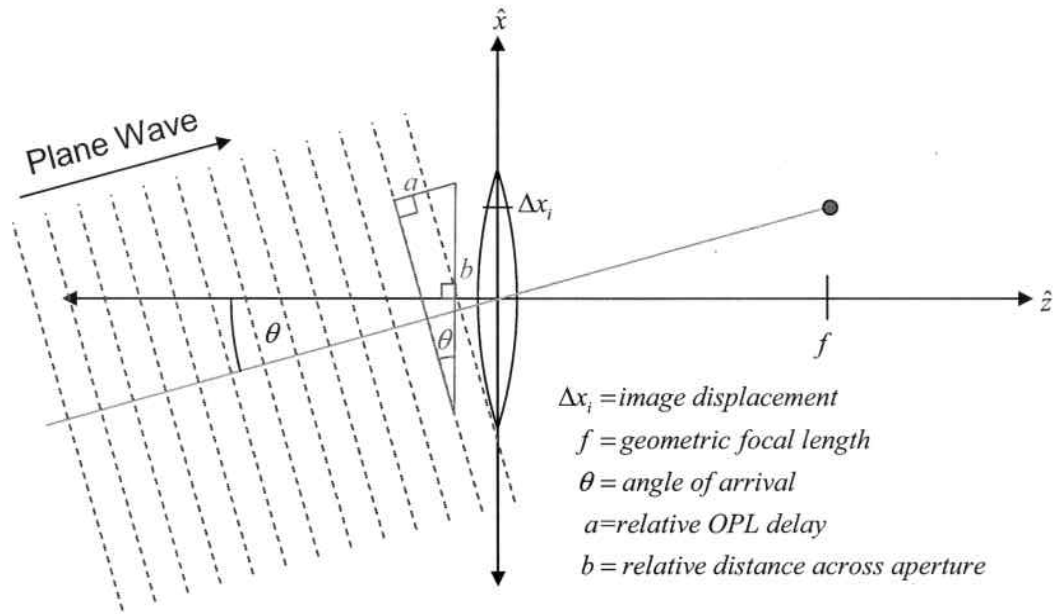\end{aligned}
\tag{3.64}
$$

Figure 3.5:   Geometric Tilt. This diagram depicts the relationship between angle of arrival and image displacement from the optical axis.

where $k = \frac{2\pi}{\lambda}$ is the propagation constant for free space. It follows from our definition of geometric tilt, that the phase over the aperture due to α_g is given by

$$\varphi(x, y) = x\alpha_g. \tag{3.65}$$

From (3.2), the corresponding amount of unscaled Zernike tilt is

$$\alpha = \iint_A \varphi(x, y) x\, dx\, dy$$
$$= \alpha_g \iint_A x^2\, dx\, dy. \tag{3.66}$$

61

Transforming from rectangular to polar coordinates, by making the substitutions, $dxdy = rdrd\theta$ and $x = r\cos(\theta)$, yields

$$
\begin{aligned}
\alpha &= \alpha_g \int_0^R \int_0^{2\pi} r^3 \cos^2(\theta) d\theta dr \\
&= \alpha_g \int_0^R r^3 \int_0^{2\pi} \frac{1 + \cos(2\theta)}{2} d\theta dr \\
&= \alpha_g \int_0^R r^3 \frac{1}{2} \left[\theta + \frac{\sin(2\theta)}{2}\right]_0^{2\pi} dr \\
&= \pi \alpha_g \int_0^R r^3 dr \\
&= \frac{\pi R^4 \alpha_g}{4} \\
&= \frac{\pi D^4 k \Delta x_i}{64 f} \\
&= \frac{\pi D^4 k w \Delta_{pix}}{64 f},
\end{aligned}
\tag{3.67}
$$

where w is a rational number representing the number of pixels by which the image is displaced in the $\hat{x}$-direction. This shows that instantaneous tilt observations can be obtained by scaling corresponding observations of instantaneous image displacement due to each source in the $\hat{x}$-direction.

3.4.3 Tabulation and Estimation.   We introduce the following maximum-likelihood estimator for covariance of observed tilt, $B_{\tilde{\alpha}}$, assuming that tilt is normally distributed. Given m independent observations of tilt for two sources, located at x_1 and x_2, such that $\Delta x = |x_1 - x_2|$, we define the estimator for tilt observed covariance as

$$
\hat{B}_{\tilde{\alpha}}(\Delta x) \triangleq \frac{1}{m} \sum_{l_1=0}^{m-1} \left(\tilde{\alpha}_{1,l_1} - \frac{1}{m} \sum_{l_2}^{m-1} \tilde{\alpha}_{1,l_2} \right) \left(\tilde{\alpha}_{2,l_1} - \frac{1}{m} \sum_{l_2}^{m-1} \tilde{\alpha}_{2,l_2} \right)
\tag{3.68}
$$

62

where $\alpha\tilde{\alpha}_{1,l}$ is the observed tilt due to source 1 from the lth image frame, and $\tilde{\alpha}_{2,l}$ is the corresponding observation of tilt due to source 2. For a particular set of estimated turbulence parameters, we define the corresponding tilt covariance to be $\hat{B}_\alpha(\Delta x)$, which is computed using the pretabulated coefficients given by (3.54). We employ the implementation of the Nelder-Mead simplex algorithm packaged with MATLAB® [19] to search for the values of l_0 and L_0 which most closely describe the observed data. For any given choice of l_0 and L_0, we solve for the unconstrained least squares estimates of C_n^2 and $\text{var}[\alpha_\eta]$, treating them as gain and bias, respectively. The cost function used for this process is normalized mean squared error in zero-mean tilt covariance:

$$\mathcal{E}_\alpha \triangleq \frac{1}{M} \sum_{i=0}^{M-1} \left[\frac{\left[\left(\hat{B}_{\alpha_{vk}}(\Delta x_i) + \hat{\sigma}_{\alpha_\eta}^2 \right) - \hat{B}_{\bar{\alpha}}(\Delta x_i) \right]^2}{\sum_{i=0}^{m-1} \hat{B}_{\bar{\alpha}}^2(\Delta x_i)} \right], \qquad (3.69)$$

where $\hat{\sigma}_{\alpha_\eta}^2 \approx \text{var}[\alpha_\eta]$ is the estimated motion variance, and $\hat{B}_{\alpha_{vk}}(\Delta x_i)$ is the tilt covariance predicted by the von Kármán model.

3.4.4 Experimental Conditions. The experiment was performed on June 15, 2006, beginning at 1544 EDT and lasted for 20 minutes. The optical path measured 100 m, and the path was 1.25 m above ground. The surface was asphalt, subject to direct solar radiation, at an equilibrium temperature of 47.22 C. The sky was clear, providing for irradiance conditions that were approximately temporally invariant. The prevailing cross-wind measured 2.0 m/s with gusts up to 2.5 m/s. The mean air temperature was 28.6 C. Relative humidity was at 27%, and the atmospheric pressure was stable at 1028 mbars. The operating wavelength was $\lambda = 532$ nm.

3.5 Results

Atmospheric turbulence is a nonstationary process. However, we treat tilt as locally stationary over short segments of time. Figure 3.6 shows a histogram of differ-

63

ential tilt observations extracted from an arbitrary block of 240 s. Another important
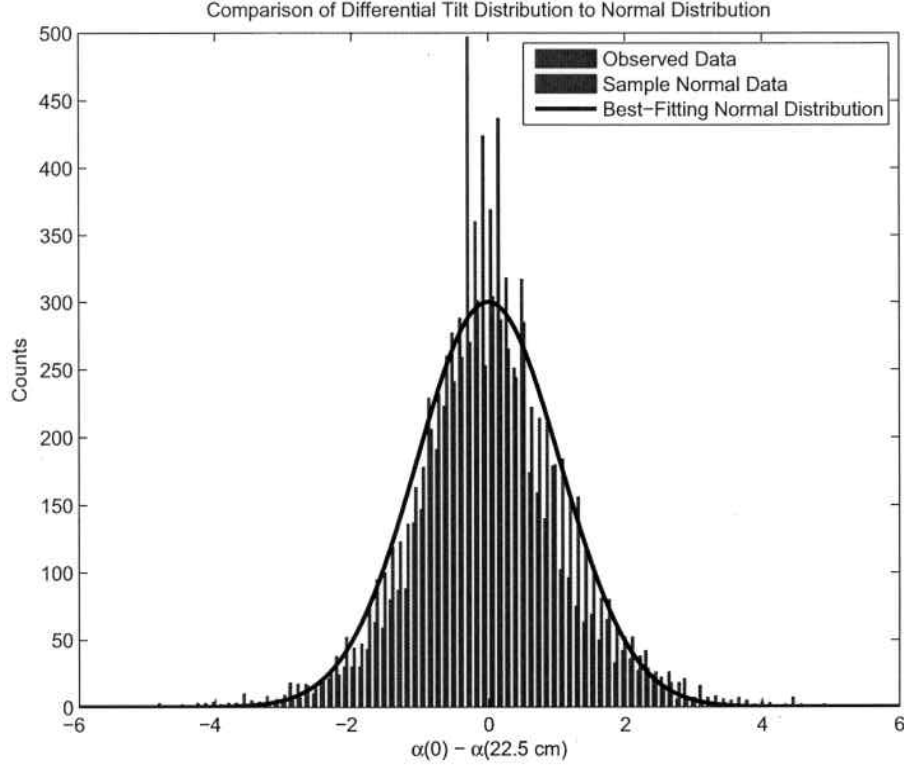

Figure 3.6:   Differential Tilt Distribution. This figure confirms that the subset of data chosen for analysis is approximately normally distributed.

point to consider is that the data is temporally correlated. Ergodicity would imply that discrete-time statistics are equivalent to ensemble statistics. For a discrete-time signal that is ergodic, we could approximate ensemble statistics by computing temporal statistics over a sufficiently long interval. Unfortunately, our signal is not ergodic, because it is nonstationary. Instead, we loosely assume that first and second-order ensemble statistics may be approximated by estimating the corresponding time statistics from a sufficiently long interval. Clearly, any data segment may be randomly reordered without affecting its ensemble statistics. The new permutation would result in a temporally uncorrelated sequence, whose members can be treated as independent observations. If the observation period were sufficiently long, then a histogram of the

data would appear unimodal and symmetric. Since Figure 3.6 shows exactly that, we have no evidence that our assumption is faulty. While, we have not validated our initial assumption, lack of any disproof is sufficient reason to continue.

Because we did not know exactly what value to use for $L_{0_{max}}$ in generating our table of spectral tilt coefficients, we produced several tables corresponding to $L_{0_{max}} \in \{1.0\,\mathrm{m}, 2.5\,\mathrm{m}, 5\,\mathrm{m}, 10\,\mathrm{m}, 40\,\mathrm{m}, 100\,\mathrm{m}\}$. Each table was produced, using a PC equipped with dual 2.4 GHz Xeon®processors with hyper-threading enabled. All four virtual processors cooperatively produce a single table in approximately 106 hours. Once produced, the tables may be reused for the same experiment under different turbulence conditions. One strategy for selecting the correct table is to start with the table corresponding to the largest $L_{0_{max}}$ and to decrease $L_{0_{max}}$ to the smallest tabulated value which is greater than the estimated value of L_0.

Figure 3.7 shows the results from estimating B_n, using $L_0 = 40\,\mathrm{m}$. The optimal solution for B_n achieved by the von Kármán covariance model for the whole data set is given in Figure 3.8. The parameters corresponding to the optimal solution for the ensemble of data are as follows:

$$C_n^2 \approx 6.01 \cdot 10^{-9}\,\mathrm{m}^{-\frac{2}{3}},$$

$$l_0 \approx 17.9\,\mathrm{mm},$$

$$L_0 \approx 15.5\,\mathrm{m}.$$

By contrast, the average parameters corresponding to the ensemble of all 240 s windows shown in Figure 3.7 are

$$C_n^2 \approx 6.10 \cdot 10^{-9}\,\mathrm{m}^{-\frac{2}{3}},$$

$$l_0 \approx 13.6\,\mathrm{mm},$$

$$L_0 \approx 14.8\,\mathrm{m}.$$

The two sets of results appear to be consistent. Figure 3.9 compares the estimated tilt covariance for the entire data set to the actual observable data. The data includes
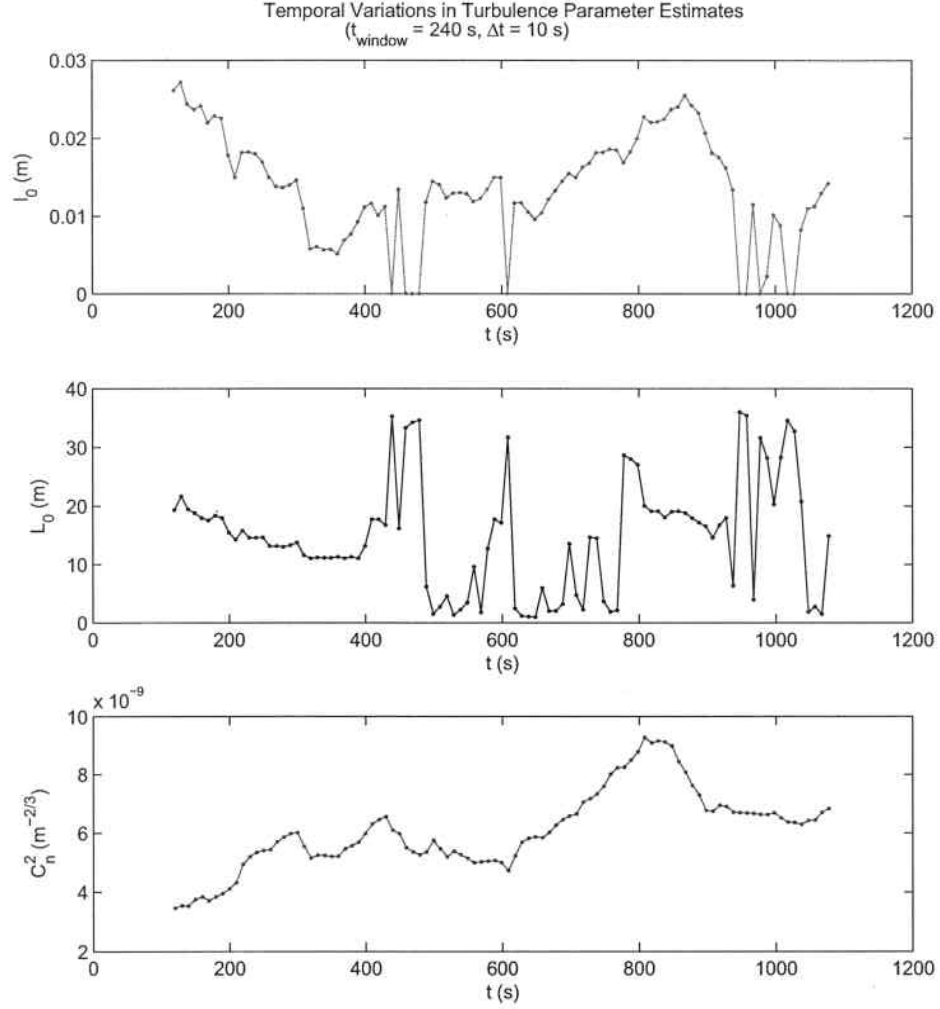
Figure 3.7: Windowed Estimates of Turbulence Parameters. This figure displays the windowed estimates of l_0, L_0, and C_n^2 corresponding to $B_n(R)$, optimized for $L_{0_{max}} = 40$ m.

the effects of platform motion. According to the figure, the von Kármán models the observed data very closely. Much prior literature has been dedicated to presenting theory and results based upon the much simpler Kolmogorov model. It has been unknown until now, how well the $\frac{2}{3}$-Power Law describes refractive index fluctuations in strong turbulence conditions near the ground. Figure 3.10 provides some initial
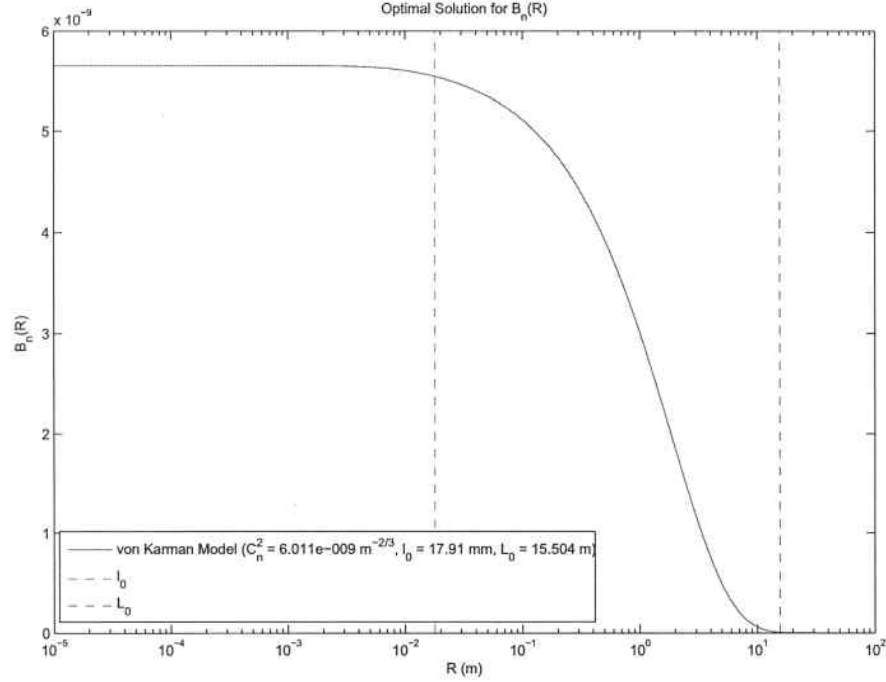
Figure 3.8: Optimal von Kármán Covariance Function. This figure displays the von Kármán B_n that optimally describes the observed data.

evidence to debunk the use of Kolmogorov theory for terrestrial imaging applications, especially where optical turbulence is likely to be strong.

3.6 Conclusions

This research could significantly impact the development of future applications in terrestrial remote sensing. We have presented a low-cost method which allows the refractive index covariance function to be *passively measured*, assuming a von Kármán model. The method does not rely on scintillation phenomenology and does not require the traditional paraxial assumption to be used. While the current theory depends on statistically homogenous and isotropic coplanar conditions, there may be immediate applications where such conditions are guaranteed. Certainly, this measurement technique offers a potential improvement over existing Kolmogorov-based techniques for optical turbulence measurement and characterization. Future
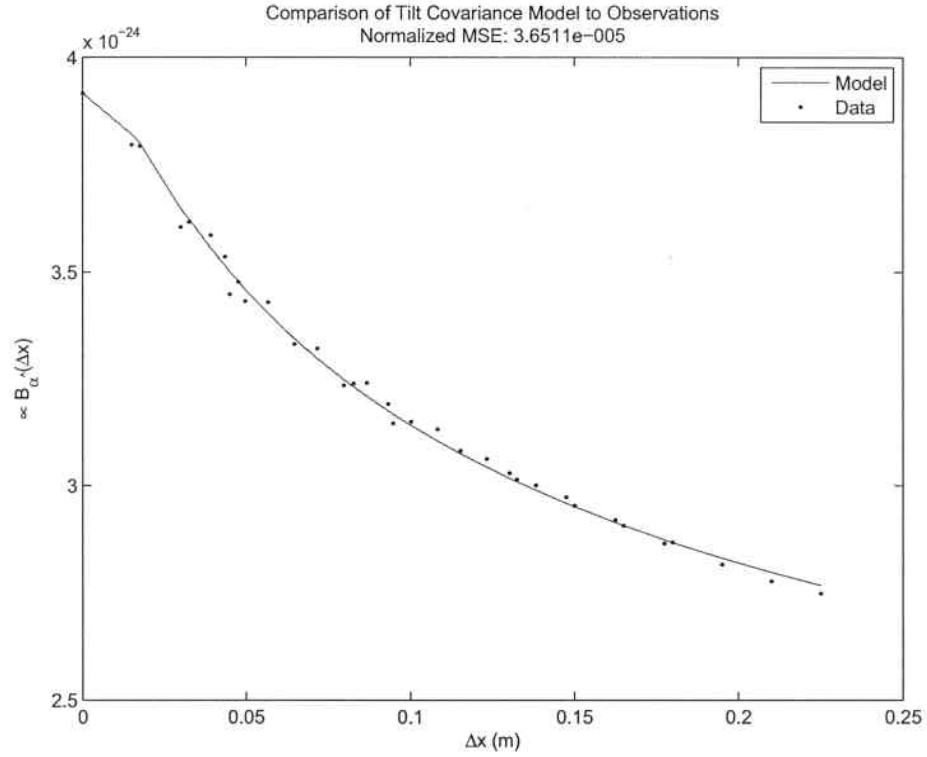
67

Figure 3.9:   Tilt Covariance. This figure compares the tilt covariance estimated directly from all observations to the tilt covariance that corresponds to B_n from Figure 3.8.

work will be directed toward establishing specific criteria for which scintillation effects can be considered negligible. The work presented in this chapter was co-sponsored by the Air Force Institute of Technology (AFIT) Department of Electrical Engineering (ENG) and by the Air Force Research Laboratory (AFRL) Electro-Optical Combat Identification Technology Branch (SNJM).
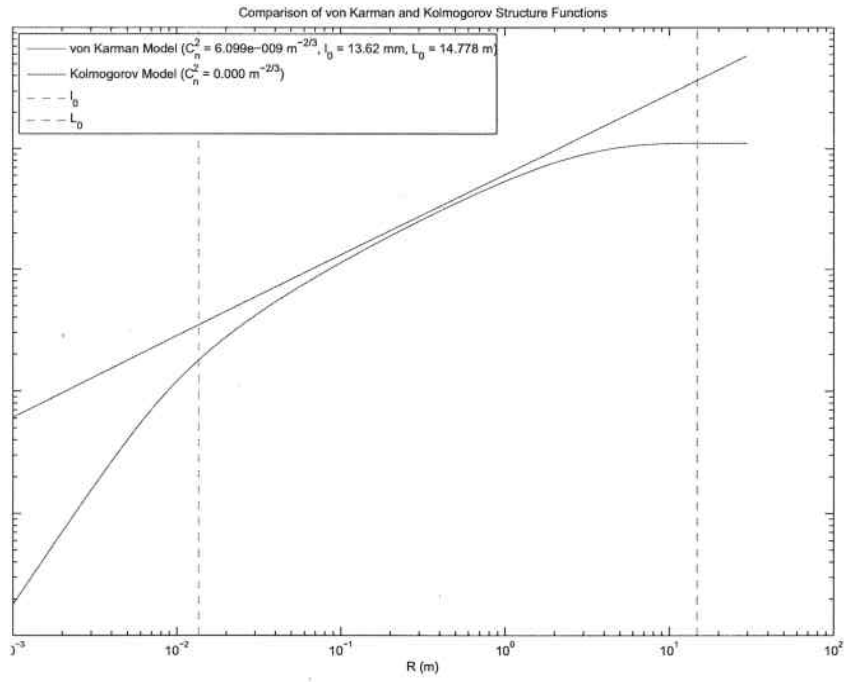
Figure 3.10:   Kolmogorov Structure. This figure compares the Kolmogorov $\frac{2}{3}$-Power Law refractive index structure function, $D_n(R)$, to the von Kármán model.

4. Summary

This dissertation documented three new contributions to help advance the state of the art in simulation, modeling, and estimation of optical turbulence. The underlying theme in this research was to revisit historical assumptions applied to previously intractable computations related to this class of problems. In Chapter 2, we presented the two contributions. The first contribution is the formalization, optimization, and validation of a modeling technique called successively conditioned rendering (SCR). The second contribution is the derivation of the covariance delineation theorem, which provides theoretical bounds on the error associated with successively conditioned rendering. It was shown how the covariance delineation theorem can be used as a computationally efficient tool for optimizing the performance of SCR algorithms. In our particular example, we compared two different SCR algorithms for simulating random phase screens. The theorem correctly predicted which algorithm would perform more accurately.

Chapter 3 documented a third contribution, by introducing a new method for estimating optical turbulence parameters, and demonstrating the method using experimental data. For our particular experiment we passively imaged an array of sources through a 100 m path at 1.25 m above the solar-heated tarmac at 28 fps. We used 10,000 samples of data assumed to be locally stationary for parameter estimation. Assuming a von Kármán turbulence model, we estimated the atmospheric parameters for these conditions to be $C_n^2 \approx 6.10 \cdot 10^{-9} \, \mathrm{m}^{-\frac{2}{3}}$, $l_0 \approx 13.6 \, \mathrm{mm}$, and $L_0 \approx 14.8 \, \mathrm{m}$.

4.1   Value to the Air Force

Collectively, these three contributions are suitable for use in several Air Force applications. Contributions 1 and 2 provide a methodology for optimizing SCR algorithms. By applying SCR to phase screen simulation, Air Force systems engineers can more efficiently and accurately characterize optical sensor performance. A few examples are laser vibrometry, imaging systems, and deconvolution algorithms.

Contribution 3 is a turnkey method for realtime estimation of optical turbulence parameters. This method can be used to support field tests, and it can also be used to characterize fade environments for operational laser communication systems. High-energy laser weapons may use this method for estimating turbulence parameters by projecting an array of low-energy laser illuminators onto a target. The imagery of the spot array could also be used to solve for the range and orientation of the target, given the target geometry. For scientific monitoring, daytime C_n^2 profiles may be obtained by placing a low-weight variant of the instrument on a weather balloon and by using a second balloon to host a passive target array. Both balloons would operate in tandem controlled ascent. Currently C_n^2 profiles are measured using thermal instrumentation. Using thermal instrumentation restricts operations to nighttime, when solar loading on the instruments is minimized.

The tilt-covariance method also has several advantages over the tri-scintillilation method recently published by Vetelino, et al [30]. The scintillation-based approach is range-limited, making long-range field tests cost-prohibitive and short-range field tests impossible for lack of detectable scintillation. Because the tilt-covariance method uses passive extended sources, high-cost sources are not needed. Optionally, light-emitting diodes (LEDs) can be used for tests conducted after twilight. Secondly, the new approach uses 34 nonlinear equations to solve for only 4 unknown parameters, while the scintillation method uses only three equations to solve for three unknowns. The redundancy helps stabilize turbulence parameter estimates in the presence of noise.

4.2 Future Work

As a natural extension to this work, the author plans to validate the estimates presented in Chapter 3 by way of 3D SCR simulation of optical turbulence. Analysis will include the effects of scintillation on the performance of turbulence parameter estimation. Simulated data will be processed through two concurrent pipelines: one which ignores scintillation, and one to include scintillation. Results will be compared to those predicted by a widely accepted technique published by Whiteley in 2002 [32].

Additional work may lead to predictive modeling of atmospheric seeing conditions as a function of time, date, location, and weather parameters. Of particular interest to astronomers is turbulence parameter profile estimation. Certain star imaging algorithms which depend on crude profile estimates of non-zero inner scale and finite outer scale may be able to use estimates of these parameters obtained from the boundary layer. One such application is proposed in [3].

Appendix A. Approximating Waves in Random Media

If we are to prescribe the use of Rayleigh-Sommerfeld (R-S) diffraction theory, we must first validate the assumptions for the case of diffraction through a turbulent medium[1]. R-S theory was developed specifically for propagation of a monochromatic wave through a homogenous and isotropic medium. In the course of this development, as presented by Goodman in [11], a scalar wave equation is derived from Maxwell's equations, under the assumption of homogenous permittivity, . By the relationship, $n = \sqrt{\frac{\epsilon}{\epsilon_0}}$, we see that this assumption is immediately violated because n is not homogenous in turbulence. Fortunately, this violation is minor because is manifested in a negligible depolarization term resulting from Earth's mildly turbulent atmosphere. Thus, the usual scalar wave equation can be made to approximate diffraction through a turbulent medium [12]:

$$\nabla^2 u(\boldsymbol{p}, t) - \frac{[n(\boldsymbol{p})]^2}{c^2} \frac{\partial^2}{\partial t^2} u(\boldsymbol{p}, t) = 0 \tag{A.1}$$

A.1 Violation of Helmholtz Equation

The next step in Goodman's development of the R-S diffraction theory necessitates that a diverging spherical wave satisfy the following Helmholtz equation for all time [11]:

$$(\nabla^2 + [k(\boldsymbol{p})]^2)g(\boldsymbol{p}, t) = 0 \tag{A.2}$$

In this expression, the propagation constant, k, is a random field defined by the relationship, $k = \frac{2\pi\nu n}{c}$, and g is the candidate Green's function describing a diverging spherical wave. Since the Helmholtz equation is an entirely spatial relationship, we define $g(\boldsymbol{p}, t_0)$ for some particular $t = t_0$ to have a phase offset of φ_0:

$$g(\boldsymbol{p}, t_0) = |\boldsymbol{p} - \boldsymbol{p}_0|^{-1} \exp\{j[k(\boldsymbol{p})|\boldsymbol{p} - \boldsymbol{p}_0| - \varphi_0]\}. \tag{A.3}$$

---

[1]The medium is also assumed to be nonmagnetic, dielectric, nondispersive, and linear. [11]

73

It is now a trivial matter to show that a diverging spherical wave does not satisfy the Helmholtz equation in a turbulent medium represented by the random field, $k(\boldsymbol{p})$. We begin by defining the Laplacian operator, ∇^2, in spherical coordinates [31]:

$$\nabla^2 \triangleq \frac{\partial^2}{\partial r^2} + \frac{2}{r}\frac{\partial}{\partial r} + \frac{1}{r^2 \sin^2(\phi)}\frac{\partial^2}{\partial \theta^2} + \frac{\cos(\phi)}{r^2 \sin(\phi)}\frac{\partial}{\partial \phi} + \frac{1}{r^2}\frac{\partial^2}{\partial \phi^2}. \tag{A.4}$$

Next, we allow k to be spatially variant and use the definition from (A.4) in applying (A.2) to (A.3). Expanding the left-hand side of (A.2) yields the following expression for the error in the electromagnetic field, expressed in spherical coordinates:

$$\Delta_{err} = g\left[-2rk\frac{\partial k}{\partial r} - \left(r\frac{\partial k}{\partial r}\right) + r\frac{\partial^2 k}{\partial r^2} + j\frac{\partial k}{\partial r}\right.$$
$$\left. + \quad r^{-1}\left(\sin^{-2}(\phi)\left[-\left(\frac{\partial k}{\partial \theta}\right)^2 + j\frac{\partial^2 k}{\partial \theta^2}\right] + j\cot(\phi)\frac{\partial k}{\partial \phi} - \left(\frac{\partial k}{\partial \phi}\right)^2 + j\frac{\partial^2 k}{\partial \phi^2}\right)\right], \tag{A.5}$$

The spatial dependencies on g and k have been dropped for convenience, and the chosen origin is $\boldsymbol{p}_0$ so that $r = |\boldsymbol{p} - \boldsymbol{p}_0|$. Ignoring this electromagnetic field error is equivalent to asserting that $\nabla k \approx \boldsymbol{0}$.

Arguably, no possible assignment of g may exist to satisfy (A.2), but such a proof is beyond the scope of this work. Instead of meticulously analyzing the existence of a perfect solution, we will simply assume any linear combination of spherical waves *approximately* satisfies the Helmholtz equation in turbulence. This is nearly equivalent to the approximation made by Goodman when by discarding the depolarization term in arriving at (A.1) [11].

A.2   Turbulence-Modified Diffraction Formula

The free-space R-S diffraction formula is given by [11]

$$u(\boldsymbol{p}_0) = \frac{1}{j\lambda_0} \int\!\!\!\int_{-\infty}^{\infty} W(\boldsymbol{p}_\perp)\frac{u(\boldsymbol{p})}{r} \exp\{jk_0 r\} \cos\left(-\hat{\boldsymbol{z}}, \boldsymbol{r}\right) d\boldsymbol{p}_\perp, \qquad (A.6)$$

where u is the scalar field, frozen in time. $\boldsymbol{p} = (x, y, 0)$ refers to a point in the plane of the aperture described by the binary window function, $W(\boldsymbol{p}_\perp)$, where $\boldsymbol{p}_\perp = (\boldsymbol{p}\cdot\hat{\boldsymbol{x}}, \boldsymbol{p}\cdot\hat{\boldsymbol{y}})$. $\boldsymbol{p}_0 = (x_0, y_0, z_0)$ is second point in free space described by the vector $\boldsymbol{r} = \boldsymbol{p}_0 - \boldsymbol{p}$. $\hat{\boldsymbol{z}}$ is the unit vector normal to the plane of the aperture pointing toward $\boldsymbol{p}_0$, and k_0 is the free-space propagation constant. Figure A.1 illustrates the geometry for (A.6). The derivation of the free-space R-S diffraction formula in (A.6) assumes that k is
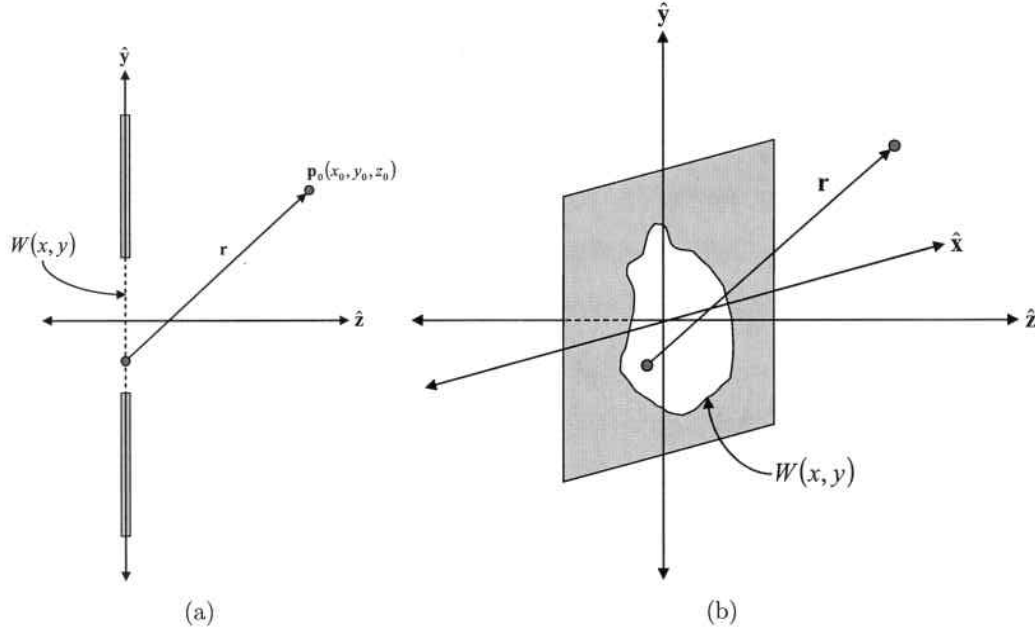

Figure A.1:   Rayleigh-Sommerfeld vacuum propagation. This figure illustrates the geometry for (A.6).

constant by setting the gradient of k to zero.

We can modify this formula to account for phase distortions associated with a turbulent dielectric. We do this by assuming that $E[k] = k_0$ and making the

substitution $k_0 r = \int_0^1 k(\boldsymbol{p} + s(\boldsymbol{p}_0 - \boldsymbol{p})) ds$, which results in the following turbulence-modified R-S diffraction formula:

$$u(\boldsymbol{p}_0) = \frac{1}{j\lambda_0 \boldsymbol{p}_0 \cdot \hat{\boldsymbol{z}}} \int\!\!\!\int_{-\infty}^{\infty} W(\boldsymbol{p}_\perp) u(\boldsymbol{p}) \exp\left\{ j \int_0^1 k(\boldsymbol{p} + s(\boldsymbol{p}_0 - \boldsymbol{p})) ds \right\} d\boldsymbol{p}_\perp, \qquad \text{(A.7)}$$

where we have also borrowed a portion of the Fresnel approximation by substituting $r^{-1} \cos(-\hat{\boldsymbol{z}}, \boldsymbol{r}) = z_0^{-1}$. It should be noted that this approximation is only valid for optical paths short enough where scintillation is negligible.

Bibliography

1. Andrews, L. C. and R. L. Phillips *et al.* "Theory of Optical Scintillation". *J. Opt. Soc. Am. A*, 16:1417–1429, 1999.

2. Andrews, Larry C. and Ronald L. Phillips. *Laser Beam Propagation Through Random Media.* SPIE Optical Engineering Press, 1998.

3. Cain, Stephen C. "Atmospheric Turbulence Profile Estimation Using a Single Laser Guide Star". William E. Thompson and Richard L. Brunson (editors), *Proceeding of Laser Systems Technology II*, volume 5413, 50–57. SPIE, Bellingham, WA, 2004.

4. Ciddor, Phillip E. "Refractive Index of Air: New Equations for the Visible and Near Infrared". *Applied Optics*, 35(9):1566–1573, March 1996.

5. Cucker, Felipe and Antonio Gonzalez Corbalan. "An Alternate Proof of the Continuity of the Roots of a Polynomial". *American Mathematical Monthly*, 96(4):342–345, 1989.

6. Dunphy, James R. and J. Richard Kerr. "Scintillation Measurements for Large Integrated-Path Turbulence". *J. Opt Soc. Am.*, 63:981–986, 1973.

7. *et al*, C. E. Coulman. "Outer Scale of Turbulence Appropriate to Modeling Refractive-Index Structure Profiles". *Applied Optics*, 27:155–160, 1988.

8. Flatté, Stanley M. and James S. Gerber. "Irradiance-Variance Behavior by Numerical Simulation for Plane-Wave and Spherical-Wave Optical Propagation Through Strong Turbulence". *J. Opt. Soc. Am. A*, 17:1092–1097, 2000.

9. Formwalt, Byron and Stephen Cain. "Optimized Phase Screen Modeling for Optical Turbulence". *Applied Optics*, 45:5657–5668, 2006.

10. Frehlich, R. G. "Intensity Covariance of a Poinnt Source in a Random Medium with a Kolmogorov Spectrum and an Inner Scale of Turbulence". *J. Opt. Soc. Am. A*, 4:360–366, 1987.

11. Goodman, Joseph W. *Introduction to Fourier Optics*. McGraw Hill, Boston, MA, 2nd edition, 1996.

12. Goodman, Joseph W. *Statistical Optics*. John Wiley and Sons, Inc., 2000.

13. Harding, Cressida M., Rachel A. Johnston, and Richard G. Lane. "Fast Simulation of a Kolmogorov Phase Screen". *Applied Optics*, 38(11):2161–2170, April 1999.

14. Hill, Reginald J. "Comparison of Scintillation Methods for Measuring the Inner Scale of Turbulence". *Applied Optics*, 27:2187–2193, 1988.

15. Hill, Reginald J. and Rod G. Frehlich. "Onset of Strong Scintillation with Application to Remote Sensing of Turbulence Inner Scale". *Applied Optics*, 35:986–997, 1996.

16. Lane, Richard G., A. Glindemann, and J. C. Dainty. "Simulation of a Kolmogorov Phase Screen". *Waves in Random Media 2*, 209–224, February 1992.

17. Martin, J. M. and Stanley M. Flatté. "Simulation of Point-Source Scintillation Through Three-Dimensional Random Media". *J. Opt. Soc. Am. A*, 7:838–847, 1990.

18. Masciadri, E. and J. Vernin. "Optical Technique for Inner-Scale Measurement: Possible Astronomical Applications". *Applied Optics*, 36:1320–1327, 1997.

19. The Mathworks, Inc, Natick, Massachusetts. *MATLAB Function Reference Volume 2: F - O*, 2002.

20. Meade Instruments Corporation, Irvine, California. *Instruction Manual: 8", 10", 12", 14", 16", LX200GPS Schmidt-Cassegrain Telescopes; 7" LX200GPS Maksutov-Cassegrain Telescope with Autostar II Hand Controller*, 2003. URL http://www.meade.com/manuals/TelescopeManuals/LXseries/LX200GPS manual.pdf.

21. Ochs, Gerard R. and Reginald J. Hill. "Optical-Scintillation Method of Measuring Turbulence Inner Scale". *Applied Optics*, 24:2430–2432, 1985.

22. Papoulis, Athanasios and S. Unnikrishna Pillai. *Probability, Random Variables and Stochastic Processes*. McGraw Hill, Boston, MA, 4th edition, 2002.

23. Peterson, Dean M. and David Mozurkewich. "Simulating Atmosphere Phase Screens for Dilute Arrays". Wesley A. Traub (editor), *Interferometry for Optical Astronomy II*, volume 4838. SPIE, 2003.

24. Roggemann, Michael C. and Byron Welsh. *Imaging Through Turbulence*. CRC Press, 1996.

25. Roggemann, Michael C., Byron M. Welsh, Dennis Montera, and Troy A. Rhoadarmer. "Method for simulating atmospheric turbulence phase effects for multiple time slices and anisoplanatic conditions". *Applied Optics*, 34(20):4037–4051, July 1995.

26. Roper Scientific, Inc., Tucson, Arizona. *Photometrics Cascade 512B Datasheet*, 2004. URL http://www.photomet.com/pdfs/datasheets/cascade/512B.pdf.

27. Strang, Gilbert. *Linear Algebra and its Applications*. Harcourt Brace Jovanovich College Publishers, Philadelphia, PA, 3rd edition, 1988.

28. Tallarida, Ronald J. *Pocket Book of Integrals and Mathematical Formulas*. CRC Press, Ann Arbor, Michigan, 2nd edition, 1996.

29. Valley, George C. "Long- and Short-Term Strehl Ratios for Turbulence with Finite Inner and Outer Scales". *Applied Optics*, 18:984–987, 1979.

30. Vetelino, Frida and Bradley Clare *et al.* "Characterizing the Propagation Path in Moderate to Strong Optical Turbulence". *Applied Optics,* 45:3534–3543, 2006.

31. Weisstein, Eric W. "Spherical Coordinates". *MathWorld–A Wolfram Web Resource.* CRC Press LLC, 1999. URL `http://mathworld.wolfram.com /SphericalCoordinates.html`.

32. Whiteley, Matthew R. "Differential-Tilt Technique for Saturation-Resistant Profiling of Atmospheric Turbulence". *SPIE Proceedings from Conference on Adaptive Optics Systems and Technology II,* 4494:221–232, 2002.

33. Wolfram Research, Inc, Champaign, Illinois. *The Wolfram Integrator, Powered by webMATHEMATICA,* 2006. URL `http://integrals.wolfram.com`.

34. Ziad, Aziz and Matthias Schöck *et al.* "Comparison of Measurements of the Outer Scale of Turbulence by Three Different Techniques". *Applied Optics,* 43:2316–2324, 2004.

Index

The index is conceptual and does not designate every occurrence of a keyword. Page numbers in bold represent concept definition or introduction.

REPORT DOCUMENTATION PAGE

Form Approved
OMB No. 0704-0188

The public reporting burden for this collection of information is estimated to average 1 hour per response, including the time for reviewing instructions, searching existing data sources, gathering and maintaining the data needed, and completing and reviewing the collection of information. Send comments regarding this burden estimate or any other aspect of this collection of information, including suggestions for reducing the burden, to Department of Defense, Washington Headquarters Services, Directorate for Information Operations and Reports (0704-0188), 1215 Jefferson Davis Highway, Suite 1204, Arlington, VA 22202-4302. Respondents should be aware that notwithstanding any other provision of law, no person shall be subject to any penalty for failing to comply with a collection of information if it does not display a currently valid OMB control number.
PLEASE DO NOT RETURN YOUR FORM TO THE ABOVE ADDRESS.

1. REPORT DATE (DD-MM-YYYY)	2. REPORT TYPE	3. DATES COVERED (From - To)
20-12-2006	Dissertation	From 1 Sept 2003- To 20 Dec 2006

4. TITLE AND SUBTITLE	5a. CONTRACT NUMBER
Modeling, Simulation and Estimation of Optical Turbulence	
	5b. GRANT NUMBER
	5c. PROGRAM ELEMENT NUMBER

6. AUTHOR(S)	5d. PROJECT NUMBER
Byron P. Formwalt	
	5e. TASK NUMBER
	5f. WORK UNIT NUMBER

7. PERFORMING ORGANIZATION NAME(S) AND ADDRESS(ES)	8. PERFORMING ORGANIZATION REPORT NUMBER
AFIT/ENG 2950 Hobson Way WPAFB, OH 45433	AFIT-DS_ENG-07-04

9. SPONSORING/MONITORING AGENCY NAME(S) AND ADDRESS(ES)	10. SPONSOR/MONITOR'S ACRONYM(S)
Richard Richmond AFRL/SNJM Bldg 622 3109 Hobson Way WPAFB, OH 45433	
	11. SPONSOR/MONITOR'S REPORT NUMBER(S)

12. DISTRIBUTION/AVAILABILITY STATEMENT

Distribution Unlimited

13. SUPPLEMENTARY NOTES

14. ABSTRACT

This dissertation documents three new contributions to simulation and modeling of optical turbulence. The ¯rst contribution is the formalization, optimization, and validation of a modeling technique called successively conditioned rendering (SCR).
The SCR technique is empirically validated by comparing the statistical error of random phase screens generated with the technique. The second contribution is the derivation of the covariance delineation theorem, which provides theoretical bounds on the error associated with SCR. It is shown empirically that the theoretical bound may be used to predict relative algorithm performance. Therefore, the covariance delineation theorem is a powerful tool for optimizing SCR algorithms. For the third contribution, we introduce a new method for passively estimating optical turbulence parameters, and demonstrate the method using experimental data.

15. SUBJECT TERMS

16. SECURITY CLASSIFICATION OF:			17. LIMITATION OF ABSTRACT	18. NUMBER OF PAGES	19a. NAME OF RESPONSIBLE PERSON
a. REPORT	b. ABSTRACT	c. THIS PAGE	None	93	Stephen C. Cain
Unclassified	Unclassified	Unclassified			19b. TELEPHONE NUMBER (Include area code) (937) 255-3636 ext. 4716

Standard Form 298 (Rev. 8/98)
Prescribed by ANSI Std. Z39.18